https://doi.org/10.5194/egusphere-2025-1928
Preprint. Discussion started: 8 May 2025

Global and regional sea-surface temperature changes over the Marine Isotopic Stage 9e and Termination IV

Nathan Stevenard[1], Émilie Capron[1], Étienne Legrain[1,2,3] & Claire Coutelle[1]

[1]Université Grenoble Alpes, CNRS, IRD, Grenoble INP, IGE, Grenoble, France.
[2] Laboratoire de Glaciologie, Université libre de Bruxelles, Brussels, Belgium.
[3] Department of Water and Climate, Vrije Universiteit Brussel, Brussels, Belgium.

Correspondence to: Nathan Stevenard (nathan.stevenard@univ-grenoble-alpes.fr)

https://doi.org/10.5194/egusphere-2025-1928
Preprint. Discussion started: 8 May 2025

Abstract. The Marine Isotope Stage (MIS) 9, occurring approximately from 300 to 335 ka, represents an important period for studying the dynamics of Earth's climate. Interest in studying this interglacial period stems from the fact that is associated with the highest atmospheric CO_2 concentrations over the last 800 ka (excluding anthropogenic CO_2 emissions). Numerous reconstructions of the sea surface temperatures (SST) are available over this time interval, but it is challenging to assess the regional and global patterns of climate variability and to infer temporal sequences of changes from numerous marine sediment records located in different parts of the world and whose chronologies originate from different dating strategies. In this study, we present the first spatio-temporal SST synthesis over the interval 300 to 350 ka, covering this interglacial period and its preceding deglaciation (Termination IV, ~335 to ~350 ka). We include 98 high-resolution SST reconstructions and we establish a common temporal framework between the selected marine records, based on the latest reference ice core chronology (AICC2023). We also homogenize the proxy-calibration strategy by applying a single method for each proxy. Chronological and calibration uncertainties are quantified using Bayesian and Monte Carlo procedures. Finally, through a Monte Carlo approach, we generate global and regional SST stacks relative to Pre-Industrial Era over Termination IV and MIS 9.

We highlight significant differences in terms of temporal variability, amplitude, and timing of changes in the SST records across the globe across the studied time interval. While the patterns of SST changes are homogeneous at basin-scale, heterogeneous interglacial SST peaks are observed across ocean basins. The interglacial surface temperature peaks in extra-tropic basins are similar or warmer than the pre-industrial period (PI), while intra-tropic areas appears to be colder relative to PI during glacial optimum. In addition, the timing in interglacial surface temperature peaks differ across the different regions. These regional temperature variations suggest that atmospheric and oceanic dynamics played a greater role than global radiative forcing in shaping the MIS 9 climate. The heterogeneous timing of changes across the different regions contribute to a smoothed global response in terms of both timing and amplitude. Consequently, we find that at a global scale MIS 9e SST was as warm as the pre-industrial period (~ -0.2°C ± 0.3°C). Converted into surface air temperatures (~ -0.4°C ± 0.6°C), this estimate agrees within the uncertainty range with previous studies based on a smaller number of records with lower temporal resolution. We also compare our results on MIS 9 and Termination IV with published SST syntheses from more recent interglacial periods (MIS 5e and Holocene) and deglacial periods (Termination I and II). We find that the global deglacial surface air warming during Termination IV is similar in amplitude (~5.3°C) to that observed during Terminations I and II. Finally, a comparison of deglacial warming rates for these three terminations to the warming trend of the last 60 years emphasizes that the rapidity of modern climate change is unprecedented within the context of these past deglaciations.

https://doi.org/10.5194/egusphere-2025-1928
Preprint. Discussion started: 8 May 2025

1 Introduction

Past interglacials represent the warm periods of the Quaternary, sometimes exhibiting as warm or warmer conditions than during the pre-industrial (PI, Past Interglacials Working Group of PAGES, 2016). Therefore, studying these intervals is helpful to better understand the interactions between the different components of the climate system in a range of temperature comparable to projected future changes (Capron et al., 2019). While the global or regional temperature variability is well constrained for the most recent interglacials such as the Holocene (0 - 11 ka; 1 ka = 1000 years; e.g. Shakun et al., 2012; Osman et al., 2021) or the Last InterGlacial (LIG, 116 - 129 ka; e.g. Capron et al., 2014, 2017; Hoffman et al., 2017), multi-millennial-scale global temperature changes for older interglacial periods are not available. Based on a selection of key ice core, marine and terrestrial records, the Marine Isotopic Stage (MIS) 9e (320 to 335 ka) stands out as one of the warmest interglacial of the last 800 ka (Past Interglacials Working Group of PAGES, 2016). It is also characterized by the highest atmospheric CO_2 (300.4 ppm) and CH_4 (818 ppb) concentrations levels as recorded in the EPICA Dome C over the last 800 ka (Bereiter et al., 2015; Loulergue et al., 2008; Nehrbass-Ahles et al., 2020). Relative Sea Level (RSL) estimates for MIS 9e remain poorly constrained, with values ranging from -10 ± 13 m, estimated with a Red Sea record based on a $\delta^{18}O$ record (Grant et al., 2014), to -1 ± 23 m from global $\delta^{18}O$ benthic foraminifera records (Spratt and Lisiecki, 2016). Other discrete RSL data based on coral estimate a range from -20 to -3 m (Medina-Elizalde, 2013). Additionally, Termination IV (T-IV), the deglaciation preceding MIS 9e, is marked by an exceptionally rapid sea-level rise (~4.9 m per 100 years compared to a rise of less than 3 m per 100 years for T-I and T-II), the highest of the last 500 ka (Grant et al., 2014). These factors make MIS 9e and T-IV a relevant time interval for studying climate responses to naturally high GreenHouse Gases (GHG) concentrations and rapid sea-level rise.

Current estimates of global surface temperature during MIS 9e are primarily derived from temperature stacks over longer timescales (e.g. Shakun et al., 2015; Snyder, 2016; Friedrich et al., 2016; Clark et al., 2024). For instance, Shakun et al. (2015), compiling 49 SST records over the past 800 ka, estimate that the surface ocean temperature during the MIS 9e peak was slightly warmer (~1.8°C) than the late Holocene, with a deep ocean temperature ~2°C warmer than Holocene values (the warmest interglacial peak over the last 800 ka). Similar estimate of the Mean Ocean Temperature (MOT) at MIS 9e was derived from the noble gas composition of the air trapped in the EPICA Dome C ice core (Haeberli et al., 2021). More recent estimates of global temperature indicate a MIS 9e peak close to PI conditions, with estimates of 0.4 ± 2.2 (2σ; Snyder, 2016), 0.1 ± 0.6 (σ; Clark et al., 2024) or ~ -0.5 ± ~2 °C (σ; Friedrich et al., 2016) compared to the PI. However, all these global surface temperature reconstructions are based on a relatively small number of records (~20–35 records) and most of them have low temporal resolution. Also, they often rely on imprecise chronologies derived from alignments of the benthic $\delta^{18}O$ record at a given site to the LR04 benthic $\delta^{18}O$ stack (Lisiecki and Raymo, 2005) which was dated through orbital tuning and is associated with relatively large absolute age uncertainties (± 4 ka). Also, focusing on the time interval covering MIS 9 and Termination IV only, more high-resolution surface temperature records are available than those included in the compilations covering longer time-scales. However, those paleoclimatic records have been dated using various

https://doi.org/10.5194/egusphere-2025-1928
Preprint. Discussion started: 8 May 2025

climatic alignment strategies. Those limitations related to the construction of the paleorecord chronologies (discussed in length in Govin et al., 2015) prevents the investigation of the spatio-temporal structure of surface temperature changes at multi-millennial-scale over MIS 9 and the preceeding Termination IV.

In addition, the existing SST reconstructions covering the MIS 9e have been produced using a wide range of proxies as the alkenone unsaturation index ($U_{37}^{K\prime}$), the faunal assemblages of planktic foraminifera (Modern Analogue Technique, MAT), the magnesium and calcium (Mg/Ca) ratio or $\delta^{18}O$ from planktic foraminifera (hereafter called $\delta^{18}O_p$) or the biomarker Tex_{86}^{H}. However, recent improvements in proxy-calibrations (e.g. Tierney and Tingley, 2018; Malevich et al., 2019; Tierney et al., 2019) over the last decade make it difficult to directly compare "old" SST data with "new" ones, even if they are derived from a single proxy (as an example, see recent improvements of Mg/Ca calibrations in Gray et al., 2018; Tierney et al., 2019). These "old" SST records must therefore be recomputed to compare them with the most recent estimates. To summarize, the lack of temporal precision combined with the low number and resolution of aligned records from the existing SST syntheses of MIS 9e currently prevents to describe at multi-millennial scales the spatio-temporal climate changes and an exploration of the involved mechanisms such as previously done for younger time intervals (e.g. Shakun et al., 2012; Stone et al., 2016; Hoffman et al., 2017; Osman et al., 2021; Gao et al., 2024).

In this study, we present a new high-resolution SST synthesis covering T-IV and MIS 9 (300–350 ka) based on 98 high-resolution (<4 ka) records. To ensure accuracy, we revise both the SST calibrations and chronologies associated with the compiled paleoclimatic records. By running a Monte-Carlo process, we produce global, hemispheric and basin-scale annual temperature stacks over the studied period, accounting for uncertainties originated both from the SST calibrations and the dating. Hence, we describe for the first time at multi-millennial scale the regional and global SST changes over this time interval and we discuss their link to external or internal forcing.

2 Methods

2.1 SST selection

We reanalyze 98 published SST records (**Fig. 1B**; **Table S1**) from marine sediment cores to reconstruct both regional and global SST changes. A total of 77 records reflect the mean annual SST and 21 reflect seasonal SST (**Table S1**). Following Hoffman et al. (2017), a selection criterion of a published mean resolution of < 4,000 years was applied to exclude very low-resolution records. As a result, the average temporal resolution is ~1,700 years. We propose to include SST inferred from different SST proxies. Indeed, with the assumption that all reconstructed proxy-based SST values are slightly different from the real SST, mixing different SST tracers may provide a SST estimate that is less biased than if a single type of proxy is favoured. Hence, we include four proxies in this synthesis: the alkenone unsaturation index ($U_{37}^{K\prime}$), the Modern Analog Technique (MAT), the ratio of magnesium to calcium (Mg/Ca), and the oxygen isotope ($\delta^{18}O_p$) of planktonic foraminifera. Because the Tex_{86}^{H}, a bio-marker reconstructing the SST, is most often associated with sub-surface temperature

https://doi.org/10.5194/egusphere-2025-1928
Preprint. Discussion started: 8 May 2025

(e.g. Rouyer-Denimal et al., 2023) and the high-resolution records are sparse, we decide to not include this proxy in this synthesis.

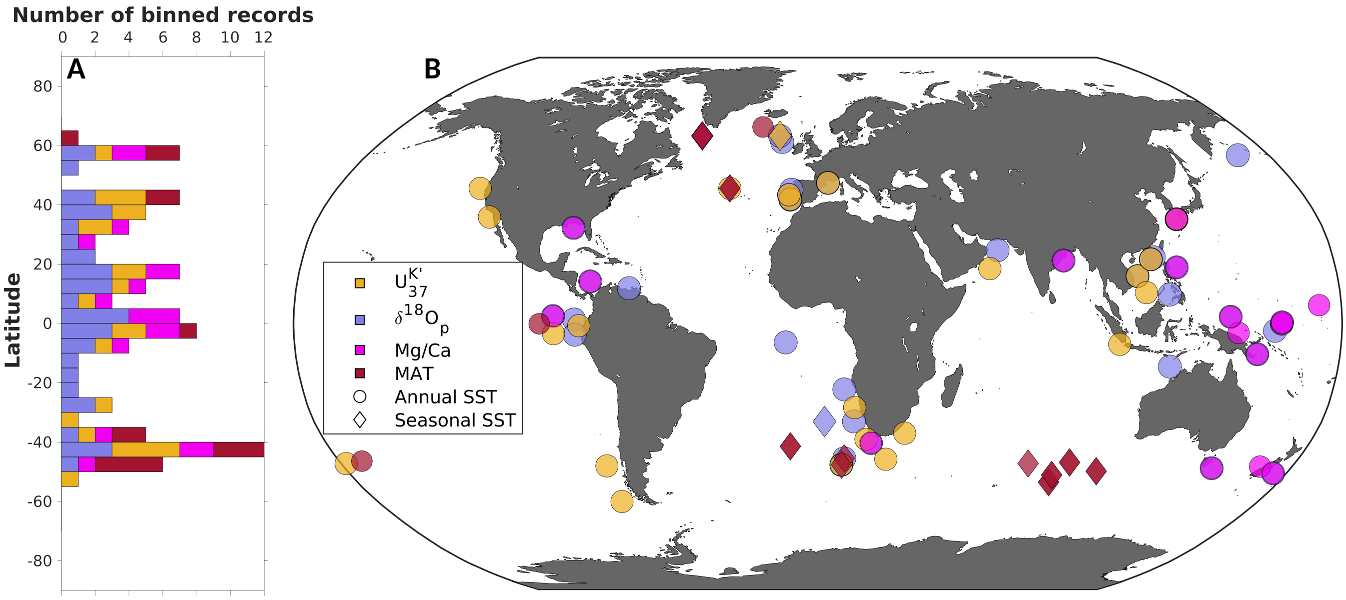

Figure 1: Location and latitudinal distributions of annual SST records. (A) Cumulative number of records per 5° latitudinal bin. (B) World map with the different types of proxies and their location. Proxies are $U^{K'}_{37}$ (yellow), $\delta^{18}O_p$ (purple), Mg/Ca ratio (pink) and MAT (dark red) for seasonal (diamonds) and annual (circles) SSTs.

2.2 SST calibrations

Based on recent advances in SST calibrations, we recalibrate the original data using a Bayesian approach which better represents the uncertainties associated with each proxy's specificities. The efficiency of this approach was demonstrated in SST syntheses for the recent period of time (0 to 24 ka, Osman et al., 2021; 18 to 21 ka, Tierney et al., 2020).

To calibrate the $U^{K'}_{37}$ data (23 records), we used the BAYSPLINE Matlab package (Tierney and Tingley, 2018). Seasonal production and slope attenuation are important features in high-temperature areas, where the $U^{K'}_{37}$ data saturate near a value of 1. Therefore, the BAYSPLINE Bayesian tool takes these features into account to produce more realistic SST reconstructions. The algorithm first calculates the SST on the basis of the Prahl et al. (1988) calibration to define the prior mean. Following Osman et al. (2021), we applied a prior standard deviation of 5°C. The BAYSPLINE package then produced a $N \times 1000$ $U^{K'}_{37}$ matrix of SST possibilities for each age N.

The Mg/Ca calibrations (17 records) were done with the BAYMAG Matlab package (Tierney et al., 2019). Since Mg/Ca is a complex paleo-thermometer due to its sensitivity to multiple environmental factors such as the calcite saturation state (Ω), salinity, or seawater pH, a linear calibration between Mg/Ca value and temperature (e.g., Anand et al., 2003) is outdated. A key advantage of using the BAYMAG calibration is that all environmental sensitivities (if known) are included

https://doi.org/10.5194/egusphere-2025-1928
Preprint. Discussion started: 8 May 2025

in the Bayesian model, avoiding the need for pre-correction of the Mg/Ca data. In this study, the prior mean is automatically defined by the model as the mean SST from an initial calibration with Anand's model (Anand et al., 2003). Following Osman et al. (2021), we applied a prior standard deviation of 6°C. The pH and salinity estimates were based on a modified function from Gray & Evans (2019), using the benthic $\delta^{18}O$ stack LR04 (Lisiecki and Raymo, 2005) as sea-level change reference. The modern calcite saturation state (Ω), pH, salinity, and temperature values were defined using two functions inherent to the BAYMAG package. The sample cleaning technique and the foraminifera species used for Mg/Ca measurements were defined based on published information. Once all the prior information was defined, we ran the BAYMAG model. This model produces an $N \times 2000$ matrix of Mg/Ca SST possibilities for each age N, then randomly subsampled to produce a smaller matrix with dimensions of about $N \times 1000$.

The $\delta^{18}O_p$ calibrations (37 records) were carried out with the BAYFOX Matlab package (Malevich et al., 2019). This package includes hierarchical models for annual, seasonal, and/or species-specific calibrations. Since we did not have sea water $\delta^{18}O$ (hereafter called $\delta^{18}O_{sw}$) estimates during the MIS 9 for all sites, we used the modern $\delta^{18}O_{sw}$ from LeGrande & Schmidt (2006) to run these calibrations. A simple ice volume correction was applied before calibration, using the benthic $\delta^{18}O$ stack LR04 (Lisiecki and Raymo, 2005) as a reference for global ice-volume changes following the (Malevich et al., 2019) correction. Finally, the prior mean was estimated either using other published SST records (published mean) if available, or using the Pre-Industrial (PI; 1870-1889) SST from HadISST (Rayner et al., 2003) as the prior mean. A fixed prior standard deviation of 10°C was applied as done in Osman et al. (2021). The ensemble of probable SSTs derived from $\delta^{18}O_p$ is a $N \times 1000$ matrix.

To our knowledge, no Bayesian approach has been developed for MAT calibrations. Most of the time, the distribution of foraminifera species is not published and only the derived SST record is available. Therefore, to propagate the uncertainties of MAT data (21 records), we conducted a Monte-Carlo analysis, randomly creating 1000 data points for each data point, following a normal distribution $N(\mu,\sigma)$. If this error (σ) was not published in the original publications, we estimated it as the standard deviation of the SST record over the period 300-350 ka. After 1000 realizations for each SST data point, the ensemble of MAT data also forms a $N \times 1000$ matrix.

For each proxy, the SST type (seasonal or annual) is defined based on the recommendation of the original studies or inferred from the calibration specifications. As a result, this synthesis comprises 74 records of annual SSTs and 20 records of seasonal SSTs.

2.3 Anomaly from the pre-industrial period

In existing SST syntheses, the SST records are commonly transferred into "anomaly" compared to a reference (e.g. Capron et al., 2014; Snyder, 2016 Hoffman et al., 2017; Tierney et al., 2020; Osman et al., 2021; Clark et al., 2024). In this study, we define the SST anomaly from the PI period. Since core-tops are rarely well preserved in our SST records and to harmonize the creation of anomalies, we defined the PI-SST (1870 to 1899 CE as used in Capron et al., 2017) by forward modelling the SST from the HadISST database (Rayner et al., 2003). This step gives 1×1000 probable proxy-values derived from the SST database. We then converted our modelled proxy-value (median value) in a 1×1000 ensemble of PI SST. This approach allows a better estimate of the proxy-SST value, which can differ from the most probable SST from the HadISST database (Rayner et al., 2003). However, we are aware of the limit of this PI reference and discrepancies of the HadISST database can exist, especially in the Southern Ocean (Gao et al., 2024). The anomaly from the PI is defined, for each record, by sorting the N^{th} ensemble of SSTs (1000 values) from least to greatest and subtracting the PI (also sorted from least to greatest).

2.4 Chronologies

In this study, we harmonize the chronologies across all marine sediment records. Due to the inability to constrain the age model with radiocarbon dates, as for the syntheses covering the most recent periods (Tierney et al., 2020; Osman et al., 2021; Gray et al., 2023), the revision of original chronologies for periods older than ~50 ka must rely on alternative strategies (Govin et al., 2012; Capron et al., 2014; Hoffman et al., 2017). For records located in high latitude areas (i.e., > 40° North or South), Govin et al. (2012) demonstrated that SST can be directly aligned with surface air temperature (SAT) records over Antarctica or Greenland for the last interglacial (LIG). For the same period, Hoffman et al. (2017) produced a new SST synthesis by aligning the benthic foraminifera $\delta^{18}O$ records to "basin references", which themselves had revised chronologies based on the alignment of SST changes to ice-core SAT variations.

In this study, a similar approach was used. As for the Govin et al. (2012) study, we first (step 1; **Fig. 2**) align the SST of four "basin reference records" from high latitudes to ice-core SAT with "*AnalySeries*" software (Paillard et al., 1996). All "basin references" (**Table S1**) contain published high-resolution SST reconstructions and benthic $\delta^{18}O$ records. Since no direct reconstructed SAT are available for Greenland from deep ice cores beyond ~130 ka, we propose to use of the Greenland synthetic curve of temperature (GL_T_syn, Barker et al., 2011). This curve is produced based on the millennial and long-term signal of Antarctica temperature records, with a 2 ka shift in order to account the "bipolar seesaw" observed between Greenland and Antarctic ice core records over the last glacial period (see Barker et al., 2011). In Capron et al. (2014), the CH_4 record was proposed as an indirect tracer for Greenland climate. Comparisons of the GL_T_syn to the CH_4 record (Loulergue et al., 2008) indicates similarities at the first order, but also some discrepancies at millennial time-scales (**Fig. S1**). These millennial-scale differences are at least partly associated with the fact that, on one side the terrestrial biosphere response to hydroclimatic changes in lower latitudes may affect the CH_4 concentrations, and on the other side that the GL_T_syn is not strictly an indicator of past Greenland temperature as illustrated with the differences observed when compared to the water isotope record from Greenland NEEM ice core over the LIG (Govin et al., 2015). With those different biases in mind, we propose to use the GL_T_syn as reference of northern high latitude temperatures, as this strategy has been already used to align marine records to ice core chronologies on older timescales (e.g. Barker et al., 2015; Hodell et al., 2015, 2023).

https://doi.org/10.5194/egusphere-2025-1928
Preprint. Discussion started: 8 May 2025

The first step thus consists in the alignment of the millennial-scale variations of SST of high latitude sites (the basin references; **Table S1**) to those of the Greenland synthetic temperature curve (Barker et al., 2011) and reconstructed SAT from the δD of EPICA Dome C (EDC, Jouzel et al., 2007), both on the most recent ice-core chronology AICC2023 (Bouchet et al., 2023). For the U1429 site (Northwest Pacific reference; **Table S1**), we aligned the variation of the $\delta^{18}O_{notched}$ (i.e. $\delta^{18}O$ of planctik foraminifera after removing the eccentricity- and obliquity-band variance; Clemens et al., 2018) of planktic foraminifera *G. ruber*, a proxy of the East Asian monsoon, to the $\delta^{18}O_{calcite}$ stack (Cheng et al., 2016) from Sanbao cave. This $\delta^{18}O_{calcite}$ record was previously scaled to the AICC2023 chronology by simple linear interpolation using the tie-points defined by Bouchet et al. (2023). Once "tie-points" were defined (**Fig. S2**), we visually estimated the depth and age uncertainties (from a few hundreds to thousands of years) to encompass the millennial-scale events as recorded in SAT references. The depth uncertainties are, most of the time, equivalent to the depth resolution of the record. At this point, only basin references are aligned to the AICC2023 ice-core chronology (**Fig. S2**).

The second step is then to align the other sites, using both basin references and ice-core records. Three scenarii occur: (1) the site has a published benthic $\delta^{18}O$ record with sufficient resolution and is aligned to a basin reference (29 sites); (2) the site has no benthic $\delta^{18}O$ record, is located in the "high latitude areas" and is aligned to ice-core SAT reconstructions (15 sites); (3) the site has no benthic $\delta^{18}O$ record, is not located in high latitudes and is finally aligned to SST from basin references or the nearest site already aligned with the first or second method (15 sites). For each method, the age and depth uncertainties are visually defined.

The third and last step consists in running a first Bayesian age-depth model with the "*Undatable*" Matlab software (Lougheed and Obrochta, 2019) to estimate the alignment uncertainties. This software takes into account the sedimentation rate uncertainties by adding a new parameter "*xfactor*" and randomly bootstraps age-depth tie-points with the "*bootpc*" parameter. As this first bayesian age model is only to estimate the alignment uncertainty on the basis of both depth and age visual errors, we ran these Bayesian age-depth models by simulating 10^5 chronologies, with an *xfactor* of 0.1 and a no bootstrap. Following this step, we estimate the absolute age uncertainty, for each site, by calculating the quadratic sum of the alignment uncertainty, and the references uncertainties which were used. As an example, the absolute uncertainties of a site aligned to the basin reference "IODP U1429" include the site alignment uncertainties of each tie-points, the U1429 to Sanbao alignment uncertainties, the Sanbao to AICC2023 uncertainties, and the absolute uncertainties of the AICC2023 ice-core chronology. Then, we run the final Bayesian age model using "*Undatable*" (Lougheed and Obrochta, 2019), with 10^5 simulations, a "*xfactor*" of 0.1 and 15% of tie-points bootstrapped in each iteration.

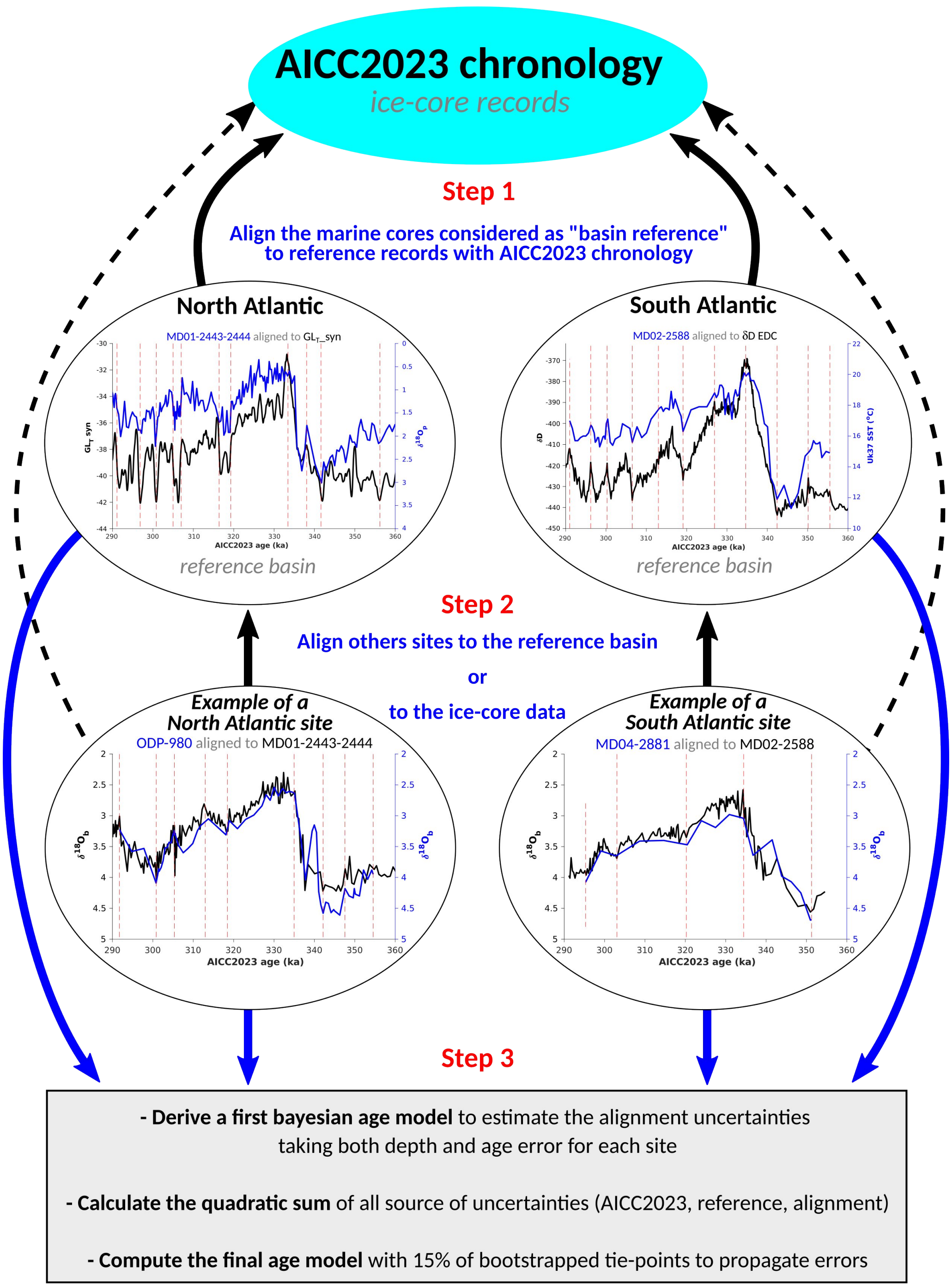

Figure 2: Description and examples of the chronology construction. In step 1 and 2, the blue curve is the record used to align to the reference (black curve). Dashed vertical lines in "Step 1" and "Step 2" represent the tie points used to align the record to the reference. For the North Atlantic example, the $\delta^{18}O_p$ from core MD01-2443-2444 (Martrat et al., 2007) is aligned to the GL_T_syn (Barker et al., 2011), and the $\delta^{18}O_p$ record from ODP-980 (McManus et al., 1999) is align to the MD01-2443-2444 one with the revised age scale.

https://doi.org/10.5194/egusphere-2025-1928
Preprint. Discussion started: 8 May 2025

As a result, the prior mean quadratic sum of all the sites range from ± 1.2 to ± 4.8 ka of uncertainties, with a mean error for all sites of ± 2.7 ka. All Bayesian age-depth models are reported in **Fig. S3**. For each depth-SST pair (*N*), we produce an ensemble of 1000 probable ages to have a $N \times 1000$ matrix.

2.5 Global and regional stack constructions

These two Bayesian processes produce ensembles ($N \times 1000$ possibilities) of both ages and SSTs for each depth-proxy pair (N) for every record. To estimate a Global Sea Surface Temperature anomaly (called ΔGSST hereafter) during MIS 5e, Hoffman et al. (2017) used a Monte-Carlo procedure. They gridded their records (SST anomalies from the PI) into a 5×5° grid and calculated the area-weighted mean and stacked 1000 Monte-Carlo iterations to construct the final global stack interpolated at regular time steps (500 or 1000 years). However, their procedure has three major drawbacks: (1) the PI from the HadISST database (Rayner et al., 2003) does not reflect the SST from a proxy and have not any uncertainties as it is a single fixed value; (2) the interpolation over-represents the high resolution ΔSST records relative to the low-resolution ones within a 5×5° grid; (3) the non-uniform geographic distribution of their records induces a bias in the global mean temperature if a large number of grids are concentrated into a single latitudinal band.

Hence, we propose here to follow an alternative strategy for computing the ΔGSST for MIS 9. Our approach is largely inspired from Osman et al. (2021) but with a few differences. The global and regional stacking processes are based on the annual SST anomaly records with their revised chronologies (see **section 2.3**). In every step of this process, we use the ensemble of data (i.e. the 1,000 probable ages and SST for each age-SST pair) to better preserve sources of uncertainties. The first step of the Monte-Carlo process involves in a random redrawn of Nth age-SST ensembles to produce different age-SST in each iteration. We also added a random normally distributed $N(0,0.5)$ error to account for laboratory precision uncertainties (Osman et al., 2021). The second step, for each time bin (500 years around the targeted date), consists of defining: i) a site mean (regardless the proxy used), ii) a random grid (between 2 and 5°) mean, and iii) a random latitudinal mean (between 2.5° and 20°). These processes reduce the impact of the spatial distribution of the sites, and the random factor provides an opportunity to account uncertainties in the spatial “choice” of the grid and latitudinal bands. In the third step, we define the ΔGSST as the mean of all latitudinal band averages and scaled it as Global Mean Surface Temperature (i.e. “air” temperature, ΔGMST) by applying a random factor between 1.5 and 2.3 (Snyder, 2016; Tierney et al., 2020; Osman et al., 2021). These values come from a comparison between ΔGSST and ΔGMST from glacial maximum climate states as simulated by climate models (Snyder, 2016). This Monte-Carlo process was repeated 10,000 times to propagate errors. At each iteration, regional stacks were also created. These stacks are based on a hemispheric scale (North, Tropics and South) or basin scale (North Atlantic, North Pacific, Equatorial Pacific, South Atlantic, Indian Ocean and South Pacific).

https://doi.org/10.5194/egusphere-2025-1928
Preprint. Discussion started: 8 May 2025

3 Results

3.1 Spatio-temporal evolution of individual ΔSST records

In this section, we describe the spatio-temporal changes inferred from our new global-scale compilation of annual and seasonal SST anomalies relative to the PI period. **Figures 3** and **4** show each record time-binned every 500 years based on the age-SST ensembles together with the uncertainty envelope representing the σ error (standard deviation) for each time bin.

3.1.1 North Atlantic Basin

17 records from 10 sites are available to describe the temporal, spatial and timing of temperature changes in the North Atlantic basin over the T-IV and MIS 9. Most of the records are located in the eastern side of the basin, two sites are located in the central North Atlantic (DSDP-607 and U1313) and one in the North-western part (U1305).

The overall structure of SST temporal changes is similar over all the records as they are marked by a minimum SST value (i.e. glacial conditions) occurring during the period preceding T-IV, a fast increase over the deglacial period, an interglacial peak or plateau and finally a cooling phase, sometimes marked by a millennial-scale strong cooling at the end of the glacial inception. The only exception is the DSDP-607 SST record, which exhibits a continuous warming of summer and winter temperatures during the deglaciation. Intriguingly, this DSDP-607 site is located at the same site as the IODP site U1313, which shows annual temperatures following the general pattern of variability as described above.

Glacial temperatures in the North Atlantic basin vary between -11 and -5°C relative to PI. The deglacial warming exhibits a range of 2.5 to 12°C (mean of ~7°C) to reach the interglacial peak or plateau. These interglacial conditions indicate, for most records, warmer temperatures compared to the PI, with a range between -2 to 4.5°C (mean of ~1.5°C).

The East and West subpolar North Atlantic (U1305, ODP-982, ODP-980) appear to warm earlier than the other sites and reach an interglacial peak between 338 and 340 ka. Other sites exhibit an interglacial peak at around 334-335 ka, with the exception of the DSDP-607 site which reaches the interglacial conditions at 331 ka.

The sites with multiple SST records indicate a similar range of variability (within the SST uncertainties). IODP site U1305 shows a consistent signal between the four records during the interglacial plateau, but also discrepancies before and after it. The case of core MD03-2699 shows the reverse scenario, with consistent values between the two records during the glacial maximum, but significant differences (~3.5°C) during the interglacial period.

3.1.2 North Pacific basin

We isolate the North Pacific from the equatorial one, keeping 13 SST records (8 sites; **Fig. 3**) for this basin. Among these records, two are located in the eastern part of the basin (ODP-1012 and ODP-1020), one in the central North (MD01-2416), while the others are located in the western part of the basin including two sites in the China Sea (ODP-1144, ODP-1146 and MD05-2901).

https://doi.org/10.5194/egusphere-2025-1928
Preprint. Discussion started: 8 May 2025

The temporal structure of the records is characterized by a glacial "maximum", clearly marked in the eastern part of the basin, but sometimes hidden by the prior variability (**Fig. 3**). Except for the $\delta^{18}O_p$-based SST record of core MD06-3074B, the deglacial warming is continuous. The $U^{K\prime}_{37}$–based SST records from ODP sites 1020 and 1012, and IODP site U1429 exhibit two steps during the deglaciation: one characterized by slow and continuous warming, the other by an abrupt warming up to the interglacial conditions. The interglacial is rarely marked by a peak (ODP-1012, Mg/Ca from U1429) and is most often a plateau followed by a slow cooling. An exception is the $\delta^{18}O_p$-based SST record from MD06-3074B, which exhibits neither an interglacial plateau nor peak.

Glacial maximum temperatures cover a large range from -8 to 2°C relative to the PI (**Fig. 3**). The deglacial warming ranges from 2.5 to 7°C (mean of ~4.5°C) and reaches the interglacial peak or plateau. This latter period is characterized by highly heterogeneous temperatures ranging from -2 to 8°C (mean of 2°C) relative to the PI. After the optimum, sites ODP-1144, ODP-1146, U1429, ODP-1012, MD05-2901 and MD06-3074B (Mg/Ca-based SST record) exhibit temperatures throughout the glacial inception within the range estimated for the PI.

While we observe some heterogeneous SST amplitudes, the timing of the changes is relatively homogeneous (**Fig. 3**), with the exception of the $\delta^{18}O_p$-based SST record of core MD06-3074B. For the two sites located in the eastern part of the basin, deglaciation starts at around 341 ka. For the other sites, it starts at approximately ~338 ka. The interglacial conditions are attained between 331 and 334 ka, within the range of the chronological uncertainties.

For sites with multiple SST records, the variability often differs in terms of shape (e.g., MD06-3074B or ODP site 1146) or amplitude (e.g., IODP site U1429, ODP site 1146, MD06-3074B, and MD05-2901). IODP site U1429, with three SST proxies, shows a consistent SST signal among them, except for anomalously warmer conditions (up to 9 °C warmer than the PI) during the interglacial peak recorded in the Mg/Ca-based SST record. We note that the SST from $\delta^{18}O_p$-based SST records in the Northwest Pacific (primarily in the China Sea) show warmer conditions during the glacial period than the other sites or proxies.

3.1.3 Equatorial Pacific

We define the Equatorial Pacific (between 10°N and 10°S) with 20 SST records (15 sites; **Fig 3**). The eastern Equatorial Pacific is represented with the ODP sites 677, 846, 1239, and cores TR163-19, RC13-110 and V19-30. Other sites are located west of the basin and two sites (ODP-1143 and MD97-2141) are in the China Sea.

https://doi.org/10.5194/egusphere-2025-1928
Preprint. Discussion started: 8 May 2025

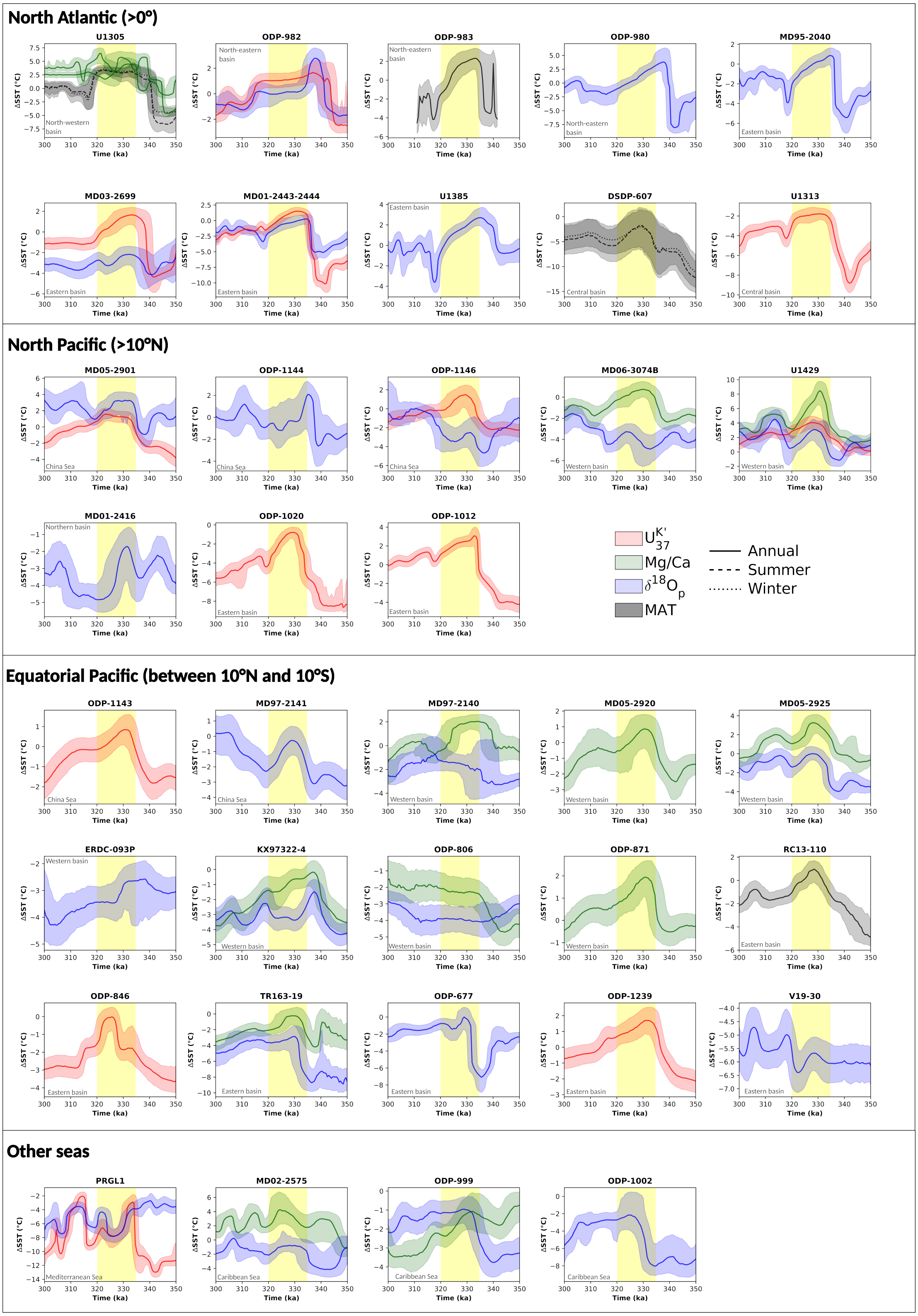

https://doi.org/10.5194/egusphere-2025-1928
Preprint. Discussion started: 8 May 2025

Figure 3: SST anomalies relative to PI for sites located in the North Atlantic, North Pacific, Equatorial Pacific and "Other seas". The SST proxies are the $U_{37}^{K'}$ (red), the Mg/Ca ratio (green), the $\delta^{18}O_p$ (blue), the MAT (black). These records are mixed between annual (solid lines), summer (dashed lines) and winter (dotted lines) SSTs. All records are time-binned every 500 years to take into account the age uncertainties. Yellow boxes represent the "optimum" interval as suggested by ice-core records. All records exhibit an envelop, that is the σ uncertainty taking both age and SST uncertainties.

The six sites from the eastern basin exhibit similar temporal variability, with the exception of the ODP site 677 SST record which shows a strong cooling before the deglacial warming and core V19-30 where the MIS 9e peak is missing. Other eastern sites exhibit gradual warming, without a marked glacial maximum (or earlier than 350 ka). The end of the deglacial period is marked by a particularly fast warming in the record from ODP site 846. Once the interglacial plateau or peak is attained, the SST gradually cools during the glacial inception, except for the ODP site 846 where a strong cooling is visible after the optimum. On the other side (western) of the basin, the temporal variability is highly heterogeneous. In particular, a few $\delta^{18}O_p$-based SST records from sites off the New Guinea coast exhibit variability that deviates from the regional pattern in terms of variability. However, except for these records and the $\delta^{18}O_p$-based SST from core MD05-2925 which shows an abrupt warming, the other SST records exhibit a glacial "maximum" followed by a gradual deglacial warming. The optimum is partially a plateau (or pseudo-plateau) and partially a peak. This optimum is followed by a gradual cooling during the glacial inception, except for the ODP site 806, which tends to gradually warm.

The eastern sites show glacial temperatures ranging between -8 and -3°C at their minimum. The deglacial warming range varies between 3.5 and 7°C (mean of 5°C) for the eastern part of the Equatorial Pacific. The interglacial values are generally slightly colder than or equal to the PI period, except for the two sites RC13-110 and ODP-1239. For the western side of the basin, the temperature during the glacial maximum (if well defined) varies between -8 and 0°C (mean of -3°C) relative to the PI. The deglacial warming ranges between 1 and 6.5°C (mean of ~3.5°C). The SST during the interglacial peak or plateau is heterogeneous, with estimates varying from -3 to 3°C.

In the eastern basin, the deglacial warming starts at different dates, from ~ 348 ka (RC13-110 and ODP-846), ~ 343 ka (ODP-1239) or ~336 ka (TR163-19 and ODP-677). Despite this heterogeneity in deglacial warming, the climatic optimum is attained at around ~331 ka for all eastern sites, except for the ODP site 846 which exhibits a late interglacial plateau starting at ~328 ka. The duration of this optimum is, however, similar (about 3 to 4 ka) between these sites. In the western basin, SST records indicate a deglacial warming starting at around 341 ka, with a few exceptions ($\delta^{18}O_p$ from TR163-19 and ODP-871 records) which start at ~339 ka. The optimum is generally attained at around ~332 ka, but some sites (ERDC-093P, MD97-2140, MD05-2925 and KX97322-4 records) exhibit an earlier interglacial peak or plateau at around ~338 ka. The duration of the optimum conditions is generally about ~5 ka, but three sites (TR163-19, MD05-2925 and MD97-2140) show longer plateaus lasting between 7 and 11 ka.

The sites with multiple SST records generally show colder SST estimations when reconstructed with the $\delta^{18}O_p$ proxy. This same tracer sometimes shows inconsistent temporal SST variability, as particularly observed in the ODP site 806 and MD97-2140 records, where no interglacial peak is recorded.

https://doi.org/10.5194/egusphere-2025-1928
Preprint. Discussion started: 8 May 2025

3.1.4 Other sites

The "other sites" (**Fig. 3**) include sediment cores located in the Caribbean Sea (MD02-2575, ODP-999 and ODP-1002) and the Mediterranean Sea (PRGL1) that cannot be integrated into the regional basins described in this section.

In the Caribbean Sea, the temporal evolution of the $\delta^{18}O_p$-based SST records shows similar patterns, with a well-defined glacial maximum, a slow deglacial warming and an interglacial plateau. However, Mg/Ca-based SST records exhibit different variability, with warmer or similar conditions during the glacial "maximum" compared to the interglacial. In the Mediterranean Sea, the deglacial warming is abrupt ($U_{37}^{K\prime}$-based SST record). The interglacial peak is directly followed by an abrupt cooling.

In the Caribbean Sea, the deglacial warming ranges from 1 to 5.5 °C (mean of 3°C). The interglacial conditions are similar to or colder than the PI (range from -2 to 4°C). In the Mediterranean Sea, the abrupt deglacial warming exhibits a 10°C difference between glacial and interglacial conditions. The interglacial, however, shows a -3°C anomaly relative to the PI.

The timing of the deglacial warming in the Caribbean Sea shows strong discrepancies, with a start between 340 and 349 ka. The date when interglacial conditions are attained is more constrained, at around ~332 ka (except for the Mg/Ca-based SST record from MD02-2575 where it is not well defined). In the Mediterranean Sea, the deglacial warming starts at ~341 ka, with an abrupt SST increase at ~335 ka. The interglacial peak is attained immediately after this warming, at 334 ka, followed by a cooling at ~332 ka.

Three of the four sites have multiple SST records (**Fig. 3**). The PRGL-1 records indicate consistent variability and values between them, with the exception of the "cold" periods (i.e. Glacial maximum and the end of the glacial inception), where the $\delta^{18}O_p$-based SST record exhibits anomalously warmer temperatures. The two sites (MD02-2575 and ODP-999) in the Caribbean Sea show strong discrepancies between their two respective records in terms of temporal variability, anomaly values and timing of changes, making it difficult to reconcile these records.

3.1.5 South Atlantic

16 SST records are located in the South Atlantic region (13 sites; **Fig. 4**) in this synthesis. These sites are concentrated in particular in the South-eastern part of the basin (**Fig. 1B**), close to the junction between the Indian and the Atlantic Oceans.

For most of the sites, the glacial maximum conditions are dated earlier than the studied period (> 350 ka) and only the SST record of core MD02-2588 shows a distinct glacial maximum. The SST records at sites GeoB1113-4, PS2489-2 ODP-1089, MD96-2085, RC12-294 and TN057-06 exhibit a continuous deglacial warming. Other sites show abrupt warming during the deglaciation. The optimum is marked by a peak in most of the sites, but a plateau is observed in the MD96-2094, ODP-1084, RC12-294, ODP-1089 and MD96-2085 records. This period is followed by a slow and continuous cooling, with a few exceptions of an abrupt cooling at the end of the optimum (ODP-1089, ODP-1090, TN057-06, GeoB1113-4 and MD96-2094).

https://doi.org/10.5194/egusphere-2025-1928
Preprint. Discussion started: 8 May 2025

As only one glacial maximum is observed, it is difficult to define a range of SST values. However, the MD02-2588 record shows temperatures -3°C colder than those of the PI. The deglacial warming amplitude ranges between 2 and 9°C (mean of ~3.5). The interglacial peak (or plateau) values range from -1.5 to 4°C (mean of ~1°C) relative to the PI. The sites that show abrupt cooling after the optimum exhibit a 2 to 4°C cooling during the glacial inception.

Due to the missing glacial maximum in most records, the timing of the start of the deglacial warming appears to be older than 350 ka. The interglacial conditions are attained between 333 and 336 ka for a few sites (MD02-2588, RC12-294, ODP-1084 and GeoB1113-4). The other sites show an earlier interglacial, mostly attained between 338 and 340 ka. The duration of the interglacial plateau is heterogeneous, ranging between ~4 ka (ODP-1090) and ~21 ka (ODP-1084), but most often around ~6 ka.

Sites with multiple SST proxies (MD96-2080 and ODP-1089) indicate inconsistent temporal variability and SST values between them. Site MD96-2080 shows similar optimum values between Mg/Ca-based and $\delta^{18}O_p$-based SST, but they are asynchronous. MAT data from site ODP-1089 does not show any warming before the interglacial peak (not covered in this record) and indicates warmer conditions compared to $\delta^{18}O_p$-based SST.

3.1.6 South Pacific

Nine SST records are located in the South Pacific (>10°S, 7 sites; **Fig. 4**). Sites GeoB3327-5 and PS75-034-2 are located in the eastern part of the basin, while the others are located off the coasts of New Zealand or Tasmania.

Except for the ODP-1172 and MD06-2986 sites, all SST records show a similar temporal variability. These variations are characterized by a well-defined glacial climate, followed by an abrupt deglacial warming. Site MD97-2120 ($\delta^{18}O_p$-based SST), however, exhibit a slightly less abrupt warming. The climate optimum appears as a short peak in most of SST records. Only the PS75-034-2 site shows an interglacial plateau. The glacial inception is characterized by a continuous cooling, except for a few sites (PS75-034-2 and Mg/Ca-based SST records from ODP-1172 and MD97-2120) which exhibit an abrupt cooling.

The glacial SST values are strongly heterogeneous, ranging from -7 (ODP-1172) to 0°C (ODP-1123) relative to the PI. The amplitude of the deglacial warming varies between 3 and 6.5°C (mean of ~5°C). The interglacial period is characterized by temperatures warmer than the PI, except for records from ODP site 1172, which indicate a -3°C (excluding $\delta^{18}O_p$-based SST record) anomaly relative to the PI. Hence, these interglacial values vary from -3 to 6°C relative to the PI.

The deglacial warming generally starts between 340 and 345 ka, with an exception at site ODP-1172 (336 ka). The interglacial maximum SST anomaly values are synchronized between the sites and are attained between 333 and 336 ka. Site PS75-034-2, the only one showing an interglacial plateau, exhibits “warm” conditions lasting for ~8 ka.

https://doi.org/10.5194/egusphere-2025-1928
Preprint. Discussion started: 8 May 2025

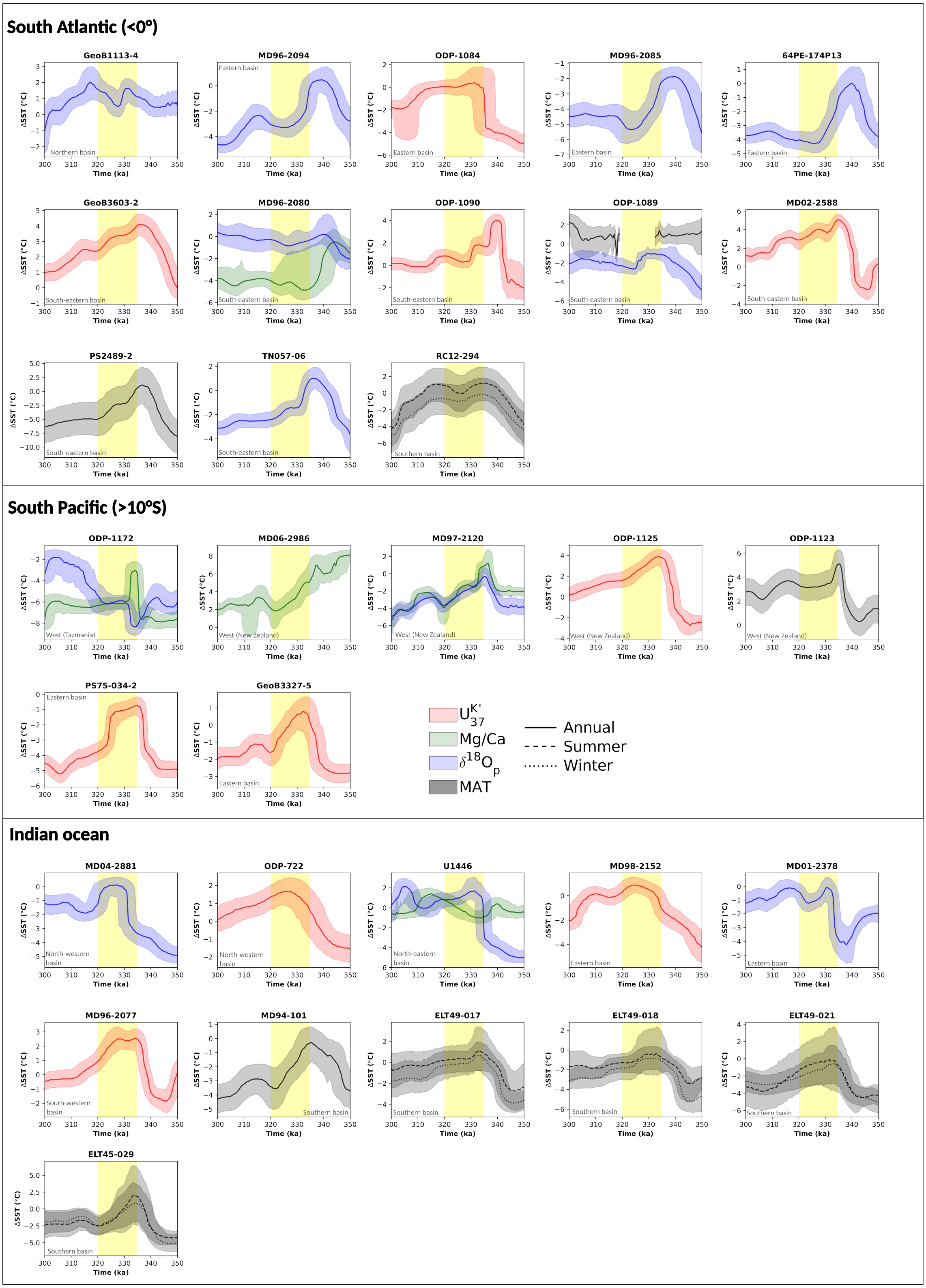

https://doi.org/10.5194/egusphere-2025-1928
Preprint. Discussion started: 8 May 2025

Figure 4: same as Fig. 2 but for the South Atlantic, South Pacific and Indian basins.

The two sites (MD97-2120 and ODP-1172) with multiple SST records show either good agreement (MD97-2120), or completely different variability and range of SST anomalies (ODP-1172). Intriguingly, the $\delta^{18}O_p$-based SST record from ODP site 1172 exhibits its coldest value during the interglacial peak, while the glacial inception shows a continuous warming. This signal strongly differs from the Mg/Ca record from the same site.

3.1.7 Indian Ocean

16 SST records are available in the Indian Ocean (11 sites; **Fig. 4**). One site (MD96-2077) is located in the southwestern side of the basin, two (MD98-2152 and MD01-2378) in the eastern side, five (ELT cores and MD94-101) in the south, and three (MD04-2881, U1446 and ODP-722) in the north.

We observe two different types of temporal structure amongst those SST records. The first type is characterized by a slow and continuous deglacial warming (the four ELT cores, MD94-101, MD98-2152 and ODP-722). The other type is characterized by an abrupt deglacial warming (MD04-2881, U1446, MD96-2077 and MD01-2378), sometimes preceded by a slow and continuous warming (MD04-2881 and $\delta^{18}O_p$-based SST record from U1446). The interglacial optimum is rarely a peak (ELT45-029, MD94-101 and MD01-2378) and is more often represented as a plateau, sometimes marked by a slight cooling. The glacial inception is characterized by a slow cooling, except for sites MD04-2881 and MD94-101 which exhibit a strong cooling at the end of the peak or plateau.

The coldest conditions before the interglacial peak or plateau are generally about -4°C (range from -5 to -1.5°C) relative to the PI. The deglacial warming ranges between 2.5 and 7°C (mean of ~4°C). The Indian Ocean appears to be warmer than 1°C compared to the PI, with all SST anomaly values equal to or greater than 0°C.
In most records, the deglacial warming starts at around ~346 ka or before 350 ka (MD94-101, MD98-2152, ELT45-029 and ODP-722). Only one record (MD01-2378) indicates a late warming at ~336 ka. The interglacial peak or plateau is attained between 330 and 334 ka, except for site the record from MD96-2077 (~336 ka). For sites exhibiting an interglacial plateau, the duration of these conditions varies between 8 and 11 ka.

Only one site (U1446) has multiple annual SST records in this basin. The $\delta^{18}O_p$-based SST record shows consistent temporal patterns, values and timing of temperature variations. However, the Mg/Ca-based SST record exhibits a very different variability, with warmer conditions during the deglacial warming than the SST derived from $\delta^{18}O_p$. Despite these differences, the glacial inception agrees in term of range of temperature between the two records, but the structures are quite differents.

https://doi.org/10.5194/egusphere-2025-1928
Preprint. Discussion started: 8 May 2025

3.2 Global and regional SST changes

The following description relies on the global and regional SST stacks (see **section 2.5**). The different sources of uncertainties related to the chronology, the SST calibration and the spatial distribution of the records are accounted for in the construction of the global and regional stacks. Hence, the dates indicated in the following sections represent the most probable dates obtained by combining all these different source of uncertainties.

3.2.1 Global scale

On a global scale, the ΔGSST and ΔGMST (**Fig. 5C**) are marked by well-defined glacial conditions at around 348 ka with temperatures that are respectively 3.0 ± 0.3 °C and 5.6 ± 1.2 °C cooler than during the PI. This cold period is followed by a ~14 ka-long continuous warming in two steps: there is a first phase associated with a slow warming rate, and then, a second phase with an increased warming rate starting at 341.5 ka and marking the onset of the deglaciation (i.e. When the global temperature start to rise sharply). The amplitudes of the deglacial warming are about ~2.7 and ~5.3 °C, respectively for ΔGSST and ΔGMST (**Fig. 5C**). The climatic optimum starts at 333 ± 0.25 ka and extends up to 328.5 ± 0.25 ka. During this period, ΔGSST and ΔGMST are respectively -0.2 ± 0.3 °C and -0.4 ± 0.6 °C relative to the PI (**Fig. 5C**).

This climatic optimum is followed by a 9 ka-long continuous cooling characterized by a ΔGSST and ΔGMST decrease of respectively 1.3°C and 2.4°C to reach values of -1.5 ± 0.4 °C and -2.8 ± 0.9 °C relative to PI. After a 2,500-years-long period of stability, the ΔGSST and ΔGMST exhibit a millennial-scale warming of reduced amplitude (~0.2 and ~0.5°C for ΔGSST and ΔGMST, respectively). Global temperatures then show a brief period of stability (~2 ± 0.25 ka), after which they continuously decrease until the end of the studied period (i.e. 300 ka). This final cooling, however, does not reach the MIS 10 glacial range of temperature values (**Fig. 5C**).

3.2.2 Hemispheric scale

On a hemispheric scale (**Fig. 5D**), the MIS 10 glacial temperature ΔSST values are colder in the extra-tropic Northern Hemisphere (NH; -3.8 ± 1.1 °C) compared to the extra-tropic Southern Hemisphere (SH; -2.7 ± 0.8 °C). Tropical (between 23° North and South) area does not exhibit a glacial maximum, and the colder temperature anomaly is -2.7 ± 0.3 °C at 350 ka. The hemispheric ΔSST stacks exhibit differences in shape, amplitude, and timing of the deglacial warming. In the SH (**Fig. 5D**), the deglaciation starts at 347 ± 0.25 ka, lasts approximately ~11.5 ka and has an amplitude of warming of ~3.0 °C. In the NH, the deglacial warming begins at 342 ± 0.25 ka, lasting for approximately ~9 ka, with an amplitude of ~3.9 °C (**Fig. 5D**). The Tropics, shows a deglacial warming longer than 19 ka, with a lower amplitude of warming of ~2.2 °C (**Fig. 5D**).

https://doi.org/10.5194/egusphere-2025-1928
Preprint. Discussion started: 8 May 2025

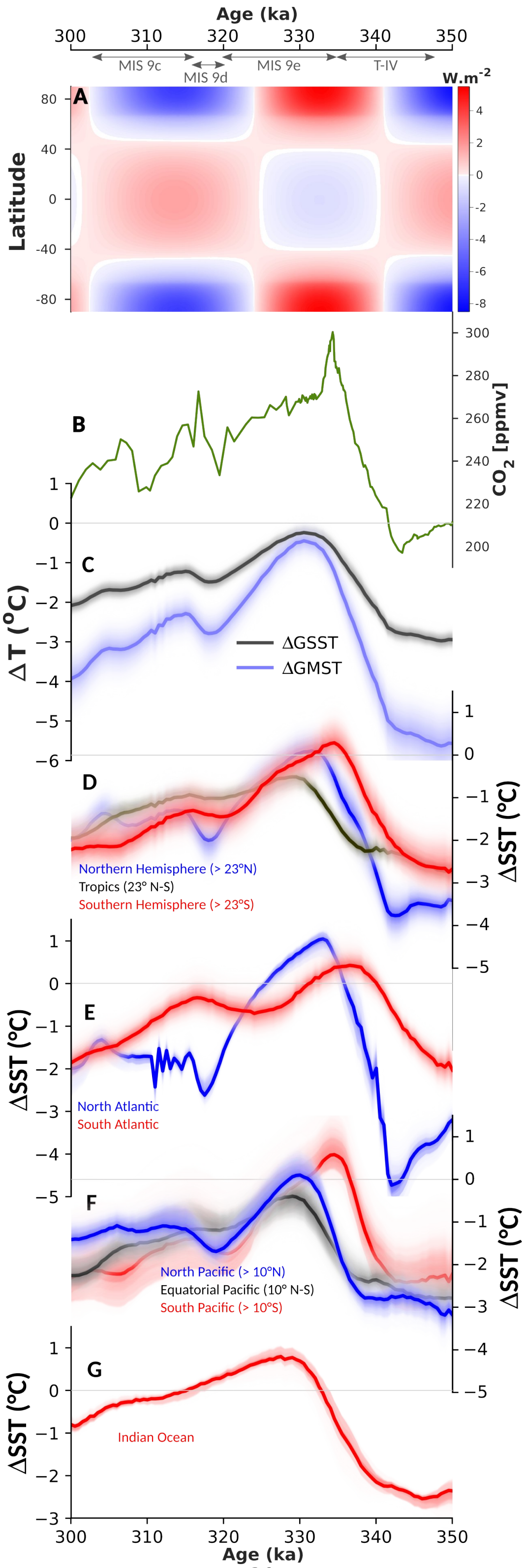

https://doi.org/10.5194/egusphere-2025-1928
Preprint. Discussion started: 8 May 2025

Figure 5: Global and regional temperature stacks over MIS 9. (A) Annual insolation anomalies from the 0-1 ka BP mean (from Laskar et al., 2004); (B) CO_2 composite from Bereiter et al. (2015) and Nehrbass-Ahles et al. (2020); (C) ΔGSST (purple) and ΔGMST (dark gray) stacks; (D) hemispheric ΔSST stacks with the NH (blue), the tropical band (black) and SH (red) anomalies; (E) Atlantic ΔSST with the North (blue) and South (red) Atlantic anomalies; (F) Pacific ΔSST with the North (blue), the Equatorial band (black) and South (red) Pacific anomalies; (G) Indian Ocean (red) anomalies. Shaded envelopes in C to G represent each percentile around the median (solid line).

As a result, the interglacial conditions are reached at 335, 333 and 331 ka in the SH, the NH and the Tropics, respectively. The maximum temperature anomaly during the interglacial peak is slightly higher in the SH and the NH to those observed for the PI period, with respectively 0.3 ± 0.7 and 0.1 ± 0.7 °C (**Fig. 5D**). However, in Tropics, temperature anomalies are lower than the PI with -0.5 ± 0.5 °C. Subsequently, SH ΔSSTs exhibits a slow cooling (-0.7 °C) up to ~326.5 ka , followed by a strong cooling (-1.0 °C) up to ~320 ka. In the NH, this cooling is ~11 ka-long and is larger (-2.1 °C), with the coolest conditions observed at ~318.5 ka. In the Tropics, a 0.5 °C cooling is observed with a shorter duration (~7 ka; **Fig. 5D**).

After these cooling periods, the SH and Tropics ΔSST are relatively stable up to ~315 ka, while the NH shows a 3 ka- warming phase of ~0.9 °C. Afterwards, the NH ΔSST exhibits a cooling (~0.7 °C) in two phases up to 300 ka (**Fig. 5D**). The SH and Tropics exhibit a continuous cooling phase about ~1.1 °C up to 300 ka.

3.2.3 Basin scale

Our regional ΔSST stacks (**Fig. 5E-G**) across the different basins of Atlantic, Pacific and Indian oceans, show similar trends in structure of temperature variability within hemispheres, but differ in terms of timing and amplitude of temperature changes.

In the NH, the MIS 10 glacial estimates indicate cooler conditions in the Atlantic than in the Pacific with values of approximately -4.7 ± 1.6°C and -3.1 ± 0.6°C respectively (**Fig. 5E-F**). This glacial maximum is attained early in the North Pacific (~348 ka), while the cold peak in the North Atlantic is only attained at ~342 ka. The deglacial in the North Pacific occurs in two steps. There is first a 0.5°C warming over a 9 ka-long phase and a second warming of 2.8°C over 7 ka. In the North Atlantic, the deglacial warming of 5.7°C occurs in about 8.5 ka. The ΔSST values at their respective climatic optimum, attained at ~333 ka and ~330 ka, are 1.0 ± 0.6°C and 0.1 ± 0.6°C (**Fig. 5E-F**) for North Atlantic and Pacific respectively. The shape of the optimum also differs, with a short an abrupt peak in the North Atlantic, directly followed by a cooling, while the ΔSST optimum in the North Pacific is more smoothed as a short plateau, lasting approximately ~3 ka. The glacial inception in the North Atlantic is characterized by a ~3.6°C cooling over ~15 ka, while it is characterized by a cooling of 1.7°C over 8.5 ka in the North Pacific. The fast warming observed in the NH ΔSST stack (**Fig. 5D**) is also well-defined in the North Atlantic, with a 2 ka temperature increase of ~1°C (**Fig. 5E**). In the North Pacific, this warming event starts 2 ka earlier than in North Atlantic. It lasts ~4 ka, but the warming amplitude is of ~0.6°C. After this millennial-scale change, the North Atlantic ΔSST are quite variable during ~5 ka with several short warming and cooling episodes associated with an amplitude of 0.4 to 0.7 °C until 300 ka (**Fig. 5E**). The North Pacific ΔSST also exhibits some variations, but the amplitude is much reduced (**Fig. 5F**).

https://doi.org/10.5194/egusphere-2025-1928
Preprint. Discussion started: 8 May 2025

The Equatorial Pacific ΔSST stack exhibits some variations that are similar to those observed in the Tropics ΔSST stack described in the previous section. The MIS 10 glacial period extends from 350 (or older) to ~338.5 ka, with ΔSST of -2.8 ± 0.5 °C slowly increasing to 2.4 ± 0.5 °C. The deglaciation is characterized by a ~8.5 ka-long warming of ~2 °C (**Fig. 5F**). The interglacial conditions are reached at 330 ka with a plateau lasting 3.5 ka. From 326 to 300 ka, the ΔSST of Equatorial Pacific exhibits a continuous cooling of ~1.8 °C.

In the SH, the Atlantic and Pacific ΔSST stacks show similar structure of variability, but differ in terms of amplitude and timing of temperature changes (**Fig. 5E-F**). The Indian Ocean ΔSST stack (**Fig. 5G**) is different in terms of temporal variability, but similar in terms of amplitude of temperature changes. The South Pacific ΔSST stack shows the highest uncertainty of all basins stacks (**Fig. 5F**). In the description below, we focus on the σ uncertainty range for this stack (not shown in **Fig. 5**). The MIS 10 glacial period is not covered in the South Atlantic stack (**Fig. 5E**). However, it extends from ~350 ka to ~342.5 ka in the South Pacific, with a minimum ΔSST values of -2.4 ± 0.5 °C (**Fig. 5F**). In the Indian Ocean, the colder values (-2.5 ± 0.3°C) are reached at ~346.5 ka (**Fig. 5G**). The deglacial warming lasts ~12 ka in the South Atlantic (and possibly longer as it is not fully recorded), with a warming amplitude of a 2.3°C (**Fig. 5E**). In the South Pacific, the deglaciation is shorter (~7 ka) and with higher warming amplitude of ~3.0°C (**Fig. 5F**). In the Indian Ocean, the deglaciation is characterized by a ~3.3 °C warming over ~16 ka (**Fig. 5G**). The interglacial conditions are reached at around ~338 ka, ~335.5 ka and 330 ka in the South Atlantic, Pacific and Indian Ocean, respectively (**Fig. 5E-G**). The ΔSST stacks show warmer conditions relative to PI during the optimum in the South Atlantic (0.4 ± 1.1°C), the South Pacific (0.6 ± 0.6°C) and the Indian Ocean (0.8 ± .0.3 °C) (**Fig. 5E-G**). The South Atlantic and Pacific basin ΔSST stacks show a cooling phase after this optimum, with durations of ~12 ka and cooling amplitudes of ~1 and ~2.3°C in South Atlantic and Pacific, respectively (**Fig. 5E-F**). After this period, short warming phases are observed, with maximum temperatures occurring synchronously between the two basins at ~316 ka. Finally, the two South Atlantic and Pacific stacks show a continuous decrease in temperature up to 300 ka, with cooling amplitudes of respectively ~1.5 and ~0.7°C (**Fig. 5E-F**). In the Indian Ocean, temperature changes after the interglacial peak are marked by a continuous cooling (~1.6 °C) until 300 ka (**Fig. 5G**).

4 Discussions

4.1 Limitations associated with our MIS 9 spatio-temporal SST synthesis

4.1.1 Limitations from the individual ΔSST records

In **Section 3.1.**, we describe in several instances an “inconsistent signal” between two SST proxies from a single site. These discrepancies, both in terms of variability and absolute values, create an uncertainty on the exact SST variations at a given site. However, when two proxies lead to inconsistent SST reconstructions, it is not always straightforward to determine which one should be preferred. For most of these inconsistent records for a given site, one of the SST values are inferred from the $\delta^{18}O_p$ proxy. We hypothesize that this discrepancy could arise from the prior $\delta^{18}O$ of seawater used for the

https://doi.org/10.5194/egusphere-2025-1928
Preprint. Discussion started: 8 May 2025

Bayesian calibration (Malevich et al., 2019), based on the $\delta^{18}O_{sw}$ synthesis from LeGrande & Schmidt (2006). In areas where this $\delta^{18}O_{sw}$ value can drastically change due to various factors such as freshwater from rivers, meltwater and rainfall, it is not surprising to observe a different pattern of SST variability and a biased signal. Without the possibility to define precisely the prior $\delta^{18}O_{sw}$ for all the sites, we maintain the same procedure for each of them. Additional issues are identified with SST derived from Mg/Ca records. This proxy is a complex paleothermometer, and the Bayesian calibration (Tierney et al., 2019) relies on several uncertain prior that can introduce bias into the records. Missing (or approximative) information, such as the cleaning method used (see Tierney et al., 2019) in original studies can lead to a less accurate calibration of the Mg/Ca ratio. So far, the MAT and $U_{37}^{K\prime}$ SST reconstructions, which do not require specific external prior (e.g. seawater properties), have not displayed major inconsistencies in SST variability; only SST derived from Mg/Ca and $\delta^{18}O_p$ exhibit such issues. We therefore propose that differences between SST estimations based on multiple proxies stem from uncertain parameters required in the calibration process. Nevertheless, inconsistent records derived from Mg/Ca or $\delta^{18}O_p$ proxies are few and are "drowned out" by other SST records during the stacking process. For this reason, we decide not to exclude any of these records.

Another limitation attached to our synthesis is related to the use of a PI SST reference originating from the HadISST database (Rayner et al., 2003). The limitations described above are not relevant for the calibration of the PI SST, as most prior (e.g. seawater properties) are well constrained for the PI period. However, Gao et al. (2024) recently compared the annual SST in the Southern Ocean of the "*piControl*" experiments from 12 climate models of the Paleoclimate Modelling Intercomparison Project Phase 4 (PMIP4) with the HadISST database for the period 1870–1899. Their findings suggest that in the Southern high latitudes (> 40°S), differences between models and data can locally range from -5 or 5°C. This highlights that uncertainties in the choice of the PI SST can bias the absolute values of anomalies reported here. Nonetheless, HadISST remains, to the best of our knowledge, the most representative estimate of monthly SST during the PI period.

4.1.2 Limitations from global and regional stacks

In this study, the use of Bayesian approaches and the Monte-Carlo processes, based on the age and ΔSST ensembles, allow us to account for all source of uncertainties (see S**ection 2.5**) and produce continuous time-series SST reconstructions without hiatus. Nevertheless, an important uncertainty remains regarding the spatial distribution of the marine records. The lack of data from the open Pacific Ocean, the central Indian Ocean, the Nordic Seas and the Western Atlantic Ocean may lead to a misinterpretation of latitudinal temperature trends. Such limitation is common when building stacks from data syntheses (e.g. Shakun et al., 2012, 2015; Capron et al., 2014; Snyder, 2016; Hoffman et al., 2017; Tierney et al., 2020; Osman et al., 2021; Clark et al., 2024) and may affect the final global ΔGSST or regional stacks. However, the stacking process used in this study minimize this unavoidable limitation (see **Section 2.5**).

Another challenge is related to the interpretation of the global ΔGSST and ΔGMST signals. Producing such stacks is very valuable for estimating the global response to natural forcing or comparing global temperature reconstructions between different periods (e.g. Snyder, 2016; Osman et al., 2021; Clark et al., 2024). However, our descriptions of hemispheric (**Section 3.2.2**) and basin scale (**Section 3.2.3**) stacks reveal significant differences in the timing of temperature changes between different regions, particularly during the deglaciation and the interglacial peak. Hence, these asynchronous changes lead to a “smoothed” global response in terms of both temporal dynamics and amplitude of variability. Considering this, it is critical to consider the individual, regional, hemispheric, and global ΔSST records all together when interpreting temperature changes across T-IV and MIS 9.

4.2 Regional temperature changes across T-IV and MIS 9

4.2.1 From glacial to interglacial conditions

The deglacial warming during T-IV is marked by major differences in the timing of regional changes (**Fig. 5D-G**). Notably, the South Atlantic appears as the first regions to warm (**Fig. 4**). This observation aligns with findings by Shakun et al. (2012) regarding the onset of the deglacial warming during the T-I, characterized by a ~2 ka lead in the Southern Hemisphere SH compared to the NH and identified as a result of the bipolar seesaw. This early deglacial warming thus appears to be a consistent feature across glacial terminations and is likely attributed to bipolar seesaw, but may also comes from the progressive export of warm and salty waters from the Agulhas Current (known as "Agulhas Leakage"), which typically flows westward into the south-eastern Atlantic basin during terminations (Peeters et al., 2004; Bard and Rickaby, 2009; Biastoch et al., 2009; Turney and Jones, 2010; Beal et al., 2011; Caley et al., 2011, 2012; Denton et al., 2021; Nuber et al., 2023). In the South Atlantic, a southward shift of westerly winds during a deglaciation (e.g. Gray et al., 2023 for T-I) likely enhanced the Agulhas Leakage, increasing the influx of warm and salty Indian Ocean waters into the South Atlantic (Denton et al., 2021; Nuber et al., 2023). This mechanism appears to be particularly important during the T-IV, amplifying SST variability and driving early warming in the South Atlantic basin. Consequently, we suggest that this early South Atlantic warming reflects an intrinsic oceanic mechanism rather than a direct response to radiative forcing. This may also explain why SH temperatures begin rising before the increase in CO_2 concentrations and Antarctic air temperatures (**Fig. 6A**), as also observed during the T-I (Shakun et al., 2012; Osman et al., 2021).

https://doi.org/10.5194/egusphere-2025-1928
Preprint. Discussion started: 8 May 2025

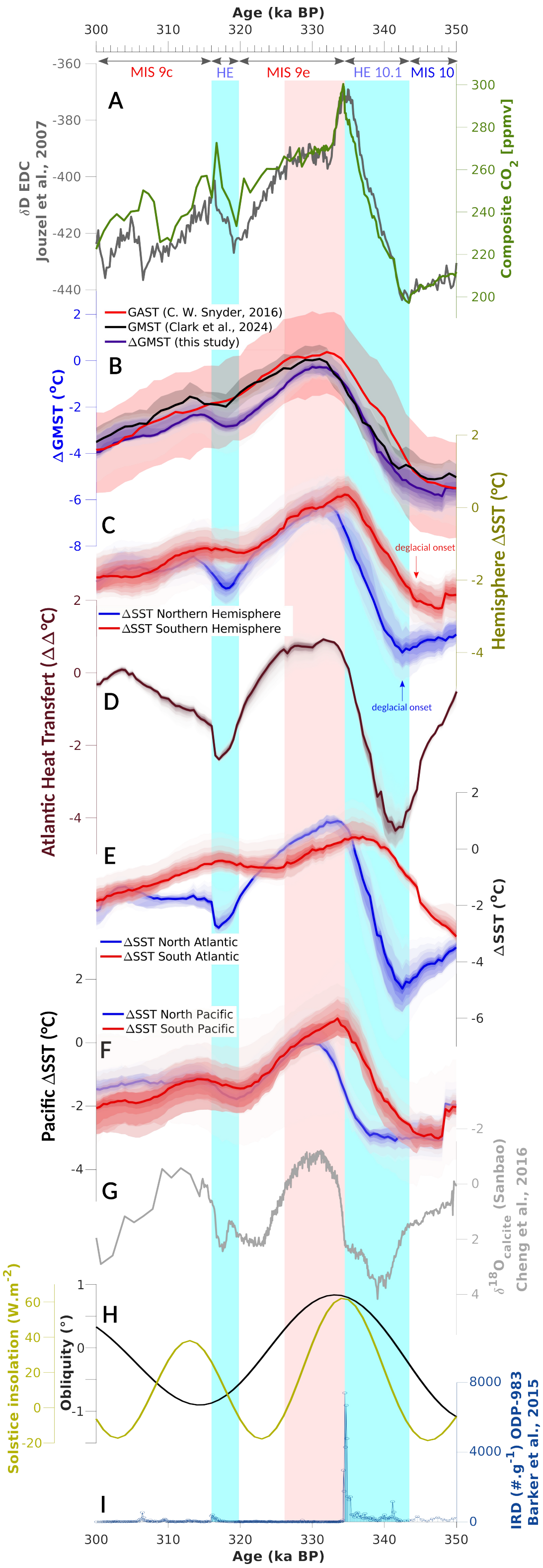

https://doi.org/10.5194/egusphere-2025-1928
Preprint. Discussion started: 8 May 2025

Figure 6: Comparisons of global and regional temperature anomaly stacks to climate records. A) δD of the EDC ice-core (grey; Jouzel et al., 2007) and composite CO_2 concentration record (green; Bereiter et al., 2015; Nehrbass-Ahles et al., 2020), B) ΔGMST (purple, this study) compared to the GAST from Snyder (2016) (red with 2σ uncertainty envelop) and GMST from Clark et al. (2024) (black with σ uncertainty envelop), C) North (blue) and South (red) hemispheric temperature stacks, D) Northern hemisphere minus Southern hemisphere temperature stacks considered as hemispheric heat transfer, E) North (blue) and South (red) Atlantic temperatures stacks, F) North (blue) and South (red) Pacific temperatures stacks obliquity (black), G) $\delta^{18}O_{calcite}$ composite record (Cheng et al., 2016) rescaled on AICC2023 following Bouchet et al. (2023), H) obliquity and 65°N solstice insolation as anomaly to present and I) IRD count of the ODP site 983 (Barker et al., 2015) rescaled on AICC2023 indicating the iceberg discharges in North Atlantic. Blue areas are related to Heinrich stadial events. Light red area marks the "optimum" of global temperatures as recorded in the ΔGMST stack. Shaded envelopes in B to F represent each percentile around the median (solid line) of our new temperature stacks.

Interestingly, North Atlantic and NH temperatures (**Fig. 6C, E**) begin increasing during the Heinrich Event (HE), as recorded by the ice-rafted debris (IRD) in the North Atlantic (**Fig. 6I**; Barker et al., 2015). This pattern mirrors observations from T-I (Shakun et al., 2012). While some North Atlantic sites show significant cooling during the HE of T-IV (**Fig. 3**), others do not, suggesting heterogeneous impacts of meltwater in the North Atlantic basin. This early warming in the NH may result as a response to the solstice insolation increase (**Fig. 6H**), that would destabilize the Northern hemisphere ice sheets and trigger the Heinrich event of T-IV as recorded in the IRD record (**Fig. 6I**).

In the North Pacific (**Fig. 6F**), late deglacial warming is likely tied to changes in the Asian Monsoon system (e.g. Cheng et al., 2016). The start of warming in the North Pacific stack coincides with the increase in East Asian monsoon rainfall, as recorded in $\delta^{18}O_{calcite}$ from Sanbao Cave (**Fig. 6G;** Cheng et al., 2016). Thus, the deglacial warming pattern observed in the North Pacific may be a response to the same mechanism affecting the East Asian monsoon, which is most likely related to the Northern high latitude insolation (Cheng et al., 2016).

We have highlighted that regional SST in the Atlantic Ocean are influenced by mechanisms associated with two important climate features, the Agulhas Leakage and HE. These events also impact the Atlantic Meridional Overturning Circulation (AMOC), either by weakening it during HE (e.g. McManus et al., 2004; Henry et al., 2016) or strengthening it through salt-water influx from the Agulhas Leakage (e.g. Beal et al., 2011; Caley et al., 2012; Nuber et al., 2023). These SST changes in the Atlantic Ocean can modify AMOC strength, thereby altering hemispheric heat transfer (Shakun et al., 2012). To illustrate this, we calculated an additional stack representing hemispheric heat transfer by subtracting Southern temperature anomalies to Northern ones (**Fig. 6E**). During the HE, the heat transfer is low, reflecting a weakened AMOC. Reduced heat transfer to the North Atlantic likely shifts atmospheric cells southward, leading to a weakened Asian monsoon (e.g. Wassenburg et al., 2021) and persistent cold conditions in the North-west Pacific (**Fig. 6F**). At ~337 ka, the heat transfer increases, suggesting an AMOC recovery despite ongoing HE conditions in the North Atlantic (**Fig. 6D**). Climate simulations by Nuber et al. (2023) confirm that salt influx in the South Atlantic during HE can drive AMOC recovery. Thus, AMOC dynamics, regulated by salt and heat fluxes (that affect density gradient between low and high latitudes; H. Stommel, 1961), emerge as a primary driver of regional deglacial temperature patterns.

To summarize, the temperature variability during the T-IV is primarily driven by radiative forcing such as insolation or CO_2 concentration increases. However, the differences observed between the different basins may be related to internal forcing such as Agulhas Leakage, massive iceberg discharges (Heinrich Event), AMOC dynamics changes or atmospheric reorganization (as illustrated by changes in East Asian monsoon).

4.2.2 From interglacial optimum to the glacial inception

Regional stacks reveal a highly heterogeneous interglacial optimum during MIS 9e, differing in timing, ΔSST values, and temporal patterns. As mentioned, early South Atlantic warming during the interglacial peak likely results from increased Agulhas Leakage (Peeters et al., 2004; Bard and Rickaby, 2009; Biastoch et al., 2009; Turney and Jones, 2010; Beal et al., 2011; Caley et al., 2011, 2012; Denton et al., 2021; Nuber et al., 2023). This warming is soon followed by cooling as heat is transferred northward *via* a strengthened AMOC (**Fig. 6D**). The plateau in hemispheric heat transfer (~333.5 ka) coincides with the North Atlantic temperature peak, underscoring the role of internal oceanic dynamics in shaping Atlantic SST variability. The subsequent cooling in both hemispheres after ~333 ka occurs as hemispheric heat transfer stabilizes, suggesting that forcing external to ocean dynamics (e.g. Insolation) becomes the dominant control over SST variability in the Atlantic Ocean (**Fig. 6A, H**). At the end of the cooling phase of the glacial inception, hemispheric heat transfer decreases, suggesting a slowdown of ocean dynamics. At the same time (317-320 ka; **Fig. 6**), a slow warming occurs in the South Atlantic while a pronounced cooling in the North Atlantic is observed (**Fig. 6E**). This bipolar seesaw millennial-scale event aligns with a typical HE SST response, as also indicated by IRD counts in the North Atlantic (Barker et al., 2015; **Fig. 6I**). This seesaw pattern underscores AMOC's critical role in redistributing surface temperatures (e.g. Stocker and Johnsen, 2003; J. Lynch-Stieglitz, 2017; Pedro et al., 2018; Davtian and Bard, 2023). The final temperature warming shift in North Atlantic at ~317 ka coincides with reduced IRD count, indicating the end of the HE.

In contrast, Pacific ΔSST changes are less abrupt (**Fig. 6F**). In the South Pacific, the interglacial peak is likely in phase with the one observed in surface air temperature recorded at EDC (**Fig. 6A**; Jouzel et al., 2007). The continuous cooling after this peak also follow Antarctic signals up to 320 ka (**Fig. 6F**). This peak leads the interglacial plateau observed in North Pacific by ~3.5 ka (**Fig. 6F**). Therefore, in the South Pacific, radiative forcing as insolation or GHG may be the major feature that drives the SST changes. However, we do not exclude that the Antarctic Circumpolar Current (ACC) strength during MIS 9e (e.g. Lamy et al., 2024) could partially influence South Pacific SST variability. In the North Pacific, the ΔSST variability during interglacial and glacial inception likely resemble to the Asian Monsoon variability, suggesting that local variability may be a direct response to the same forcing, that is likely northern summer insolation (Cheng et al., 2016).

Hemispheric ΔSST during the optimum exhibit a significant warming in extra-tropic hemispheres, with mean temperatures as warm or warmer than the PI period, while the inter-tropic areas appears to be colder (**Fig. 5D**). This observation was also made for the LIG (Hoffman et al., 2017) and is related to polar amplification (e.g. Holland and Bitz, 2003; Masson-Delmotte et al., 2010). These differences between low and high latitude temperatures are related to a larger amount of insolation forcing received in high latitudes during the optimum (**Fig. 5A**) and albedo and sea-ice positive

https://doi.org/10.5194/egusphere-2025-1928
Preprint. Discussion started: 8 May 2025

feedbacks (Capron et al., 2017). A larger obliquity can also give more contrasts in latitudinal solar energy received and reduces the sea-ice areas (e.g. Yin et al., 2021).

To summarize, the MIS 9e optimum is also primarily affected by radiative forcing and internal ones. However, the quasi-absence of AMOC changes, freshwater fluxes or changes in atmospheric circulation suggest that MIS 9e temperature variability is primarily shaped by radiative forcing with less influence of regional changes compared to T-IV.

4.3 New estimates of GMST and comparisons to previous estimates

Building on the regional patterns described above, our new ΔGMST stack offers an opportunity to refine previous estimates of ΔGMST during T-IV and MIS 9. The ΔGMST integrates temporal, timing, and amplitude variations across different regional stacks.

Our new estimate of ΔGMST provides a new perspective for studying MIS 9 and T-IV climatic response to natural forcing mechanisms (i.e. without anthropogenic forcing). As shown in **Fig. 6B**, the new ΔGMST is compared with previous global averages such as the Global Average Surface Temperature (GAST; Snyder, 2016) and Global Mean Surface Temperature (GMST; Clark et al., 2024). In terms of temporal variability, the three datasets exhibit broadly similar trends. However, a significant short-term warming event around ~317 ka (**Fig. 6B**), also recorded in the GSST stack Shakun et al. (2015), is not recorded in the GAST estimate (Snyder, 2016) and is less pronounced in the GMST (Clark et al., 2024). Therefore, our high-resolution SST synthesis made with careful attention on chronologies allows to better detect millennial-scale variability and refine the chronological framework of temperature changes over this period of time.

During the MIS 10 glacial and the cooling phase at ~305 ka, the three Global temperature estimates converge within a similar range of anomalies relative to the PI. However, the GMST from Clark et al. (2024) is ~0.6°C warmer during glacial conditions compared to our ΔGMST (**Fig. 6B**). The deglacial warming in our ΔGMST (~5.3 °C) aligns with Clark et al. (2024) (~5.2°C) and Snyder estimate (~5.9°C; Snyder, 2016). During the interglacial optimum, the previous stacks exhibit global temperature similar (from 0 to 0.3 relative to PI), while our new estimate suggests a cooler interglacial peak of -0.4 °C ± 0.6°C (**Fig. 6B**). The subsequent cooling phase shows the most notable differences between our new estimate and the previous ones, where our ΔGMST is often ~1.2°C cooler (**Fig. 6B**). While our values fall within the 2σ uncertainty of the GAST from Snyder (2016) during this period, they are outside of the lower range of the GMST uncertainties in Clark et al. (2024).

The existing MIS 9e Mean Ocean Temperature (MOT) estimate of ~2°C above the Holocene average (Shakun et al., 2015; Haeberli et al., 2021) exceeds our ΔGSST estimate by ~2.2°C (**Fig. 5C**), a difference twice as large as that observed for the LIG (Hoffman et al., 2017; Shackleton et al., 2020). The MOT is largely determined by high-latitude regions, where deep or intermediate waters are formed, and is homogenized by meridional overturning circulation (Shackleton et al., 2020). Therefore, polar SST records are essential to compare SST and MOT estimations. Unfortunately, no published SST records with sufficient temporal resolution are available for MIS 9e in Nordic Seas. Another potential factor behind these

https://doi.org/10.5194/egusphere-2025-1928
Preprint. Discussion started: 8 May 2025

discrepancies could be linked to ocean dynamics. Indeed, a slowdown of AMOC may have resulted in increased heat storage (Shackleton et al., 2020; Haeberli et al., 2021). Recent reconstruction of deep-water current strength (Stevenard et al., 2024) and Atlantic $\delta^{13}C$ synthesis (Bouttes et al., 2023), however, do not show drastic change in deep circulation during MIS 9e compared to other interglacial, excluding a heat storage related to a weakened AMOC. Therefore, deep ocean changes cannot explain such differences between ΔGSST and MOT, and this discrepancy may come from the lack of SST data in key areas, as Nordic Seas where deep water are formed, or the Indian Ocean, one of the world's largest heat absorbers during an AMOC "collapse" (Pedro et al., 2018).

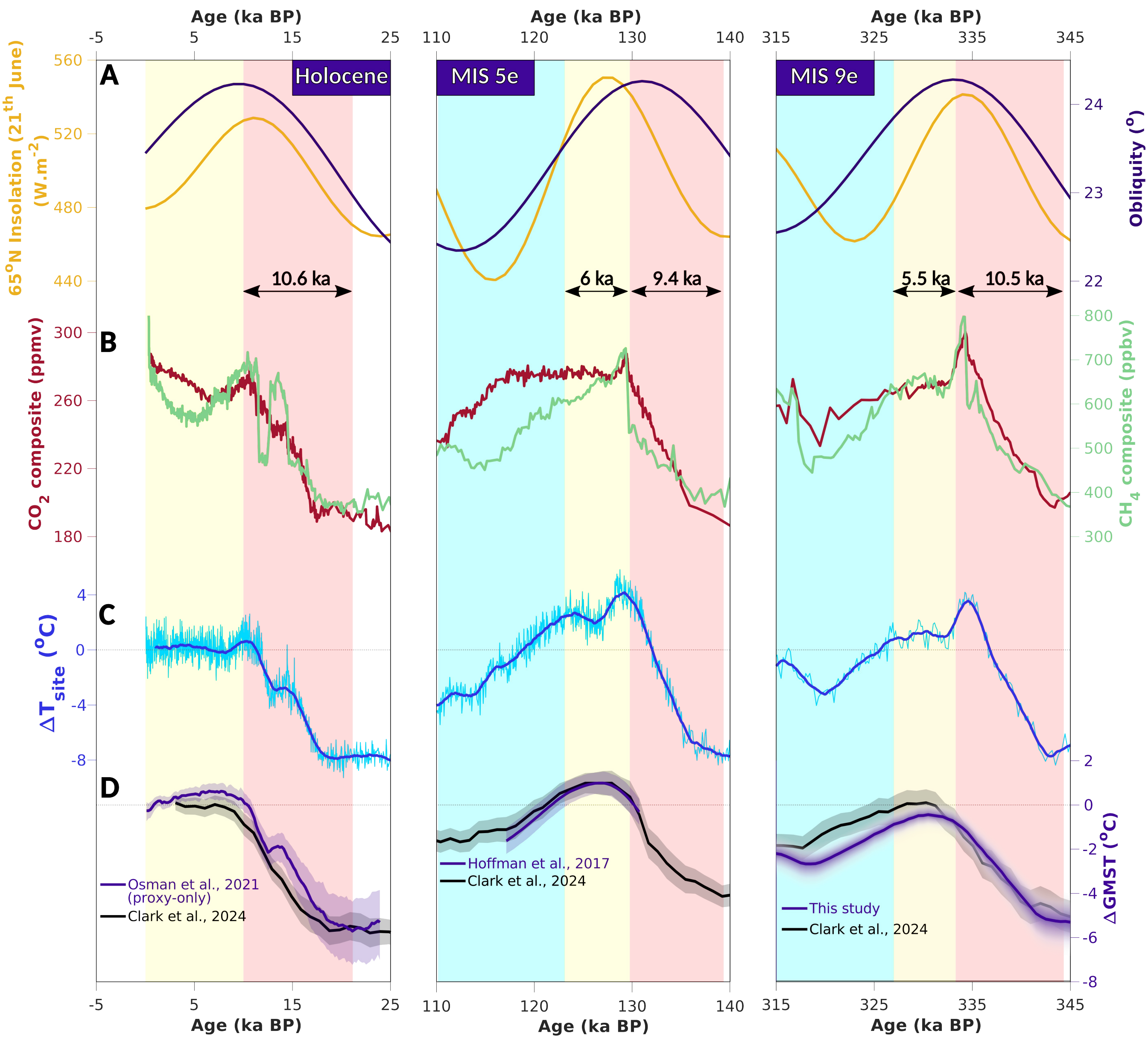

https://doi.org/10.5194/egusphere-2025-1928
Preprint. Discussion started: 8 May 2025

Figure 7: Comparison of our new MIS 9 synthesis to the Holocene and MIS 5e ones. A) 65°N summer solstice insolation (light orange, Laskar et al., 2004) and obliquity (dark purple, Berger & Loutre, 1991) variations; B) composite CO_2 (brown; Bereiter et al., 2015; Nehrbass-Ahles et al., 2022) and CH_4 (green, Loulergue et al., 2008) atmospheric concentrations; C) anomaly of Antarctic surface air temperature (light blue; Landais et al., 2021) and 2-ka moving average (blue); most recent GMST for the Holocene and T-I (Osman et al., 2021; Clark et al., 2024), the MIS 5e (Hoffman et al., 2017; Clark et al., 2024) and MIS 9e (this study; Clark et al., 2024). Note that CO_2, CH_4 and ΔT_{site} are plotted on the AICC2023 chronology (Bouchet et al., 2023). We rescale the global SST from Hoffman et al. (2017) on AICC2023 and convert it into GMST by applying the same procedure as in this study. The Osman et al. (2021) stack refers as the "data-only" rather than the estimations data-assimilated into climate model simulations. Red vertical bands are related to deglacial warming periods, yellow vertical bands to the climatic optima (visually defined) and blue vertical bands to glacial inceptions.

4.4 Comparing MIS 9 climate variability to LIG and Holocene ones

The comparison to other interglacial SST syntheses (Hoffman et al., 2017; Osman et al., 2021; Clark et al., 2024; **Fig. 7**) suggests that the warming amplitude (~5.3°C) and duration (~ 10.5 ka) of the T-IV are similar to those observed for T-I and T-II (**Fig. 7**). Intriguingly, the glacial maximum during T-II is ~2°C warmer (Clark et al., 2024) than the similar climate state observed during T-I (Osman et al., 2021) and T-IV (**Fig. 7D**).

The interglacial maximum temperature is reached approximately 2 or 3 ka after the GHG overshoot and Antarctic temperature peak, which is also observed in other past interglacials. Global mean temperatures during the optimum of MIS 9e are slightly cooler than PI conditions, the early Holocene (Osman et al., 2021) and the LIG peak (Hoffman et al., 2017; **Fig. 7**). Compared to the Holocene and MIS 5e interglacial peaks, MIS 9e exhibits a "stable" phase, whereas the others show a continuous cooling trend leading to glacial inception. Osman et al. (2021) demonstrated that this Holocene cooling phase arises from a bias in data synthesis (i.e. influenced by the geographical distribution of data), whereas assimilating these data into climate model simulations provides a more accurate estimate of global temperature changes.

In terms of orbital forcing, the MIS 9e and Holocene periods (Osman et al., 2021; Clark et al., 2024) show temperature optima occurring 2 and 3 ka after the insolation peak, respectively, whereas the LIG temperature peak coincides with the summer solstice insolation maximum (**Fig. 7A, D**). We hypothesize a link with obliquity, which affects latitudinal SST contrasts between low and high latitudes, potentially impacting AMOC strength (e.g. Zhang et al., 2017; Yin et al., 2021), and thereby heat transfer. Moreover, contrasts in latitudinal insolation (**Fig. 5A**) result in a late optimum in low latitude areas, pulling the overall global temperatures towards younger ages. The apparent synchronicity between GMST and insolation changes during the LIG (Hoffman et al., 2017; Clark et al., 2024) may be associated with the early obliquity peak, which likely reduced latitudinal contrasts during the insolation maximum.

Interestingly, the global temperature response during these three interglacial peaks is not proportional to radiative forcing, with MIS 9e exhibiting a muted response compared to the Holocene despite receiving higher insolation energy. As described in previous sections, the asynchronous regional timing of interglacial peaks results in a "smoothed" global response. The differences between the Holocene and MIS 9e can be explained by shorter regional temperature peaks during MIS 9e (**Fig. 6**), while the Holocene exhibits relatively stable hemispheric evolution (Osman et al., 2021). Thus, given the differences in temporal evolution, to better understand climate processes and feedback during past interglacials, it is crucial to look into the regional patterns of changes rather than the global-scale temperature variability.

https://doi.org/10.5194/egusphere-2025-1928
Preprint. Discussion started: 8 May 2025

MIS 9e provides a unique context to study carbon cycle forcing, as it exhibits the highest CO_2 and CH_4 concentrations of the last 800 ka (Loulergue et al., 2008; Nehrbass-Ahles et al., 2022). The increase in atmospheric CO_2 starts just before the initial deglacial warming, which is mainly modulated by the early warming in the South Atlantic. Gray et al. (2023) demonstrated that a southward shift of westerlies accompanies the atmospheric CO_2 increase during T-I, mainly by increasing the carbon release *via* upwelling in the Southern Ocean. Upwelling of deep, carbon-rich waters due to shifts in wind patterns or ocean circulation changes may have released substantial CO_2 into the atmosphere, amplifying warming trends (Sigman et al., 2010; Gray et al., 2023). This mechanism is likely the same for T-I and T-IV (and probably T-II), demonstrating the complexity of regional interactions between the different climate spheres. Interestingly, while the CO_2 overshoot during MIS 9e is larger in magnitude than that of MIS 5e, the global mean temperature response appears muted in our ΔGMST reconstructions of both MIS 5e and MIS 9e. This discrepancy may reflect the differences in regional patterns. However, as discussed in previous sections, even at the regional scale, no major local temperature peaks can be linked directly to this significant atmospheric carbon overshoot. This raises questions about the direct influence of a rapid "jump" in atmospheric CO_2 (Nehrbass-Ahles et al., 2022; Legrain et al., 2024) on regional or global temperatures, particularly given the fast subsequent decline to interglacial levels. Another explanation may be related to the millennial-scale resolution records used in these syntheses, which are unable to record the SST response to these CO_2 jumps. At present, climate model simulations for MIS 9e remain limited, making it difficult to disentangle the causes and effects of this carbon overshoot. Future simulations incorporating ocean-atmosphere carbon exchanges would offer critical insights into the carbon cycle role during MIS 9e. Such models could help elucidate how AMOC variations and Southern Ocean processes influenced CO_2 and shaped global climate responses.

4.5 Abrupt changes during T-IV compared to modern warming

The Termination T-IV was described as the deglaciation showing the most extreme sea-level rise over the last 800 ka (Grant et al., 2014). However, as mentioned in the previous sections, the amplitude of warming, estimated at ~5.3°C, is similar to those observed during T-I and T-II (**Fig. 7D**) and the MIS 9e interglacial temperature peak appears to be cooler than during the early Holocene (Osman et al., 2021) and the LIG (Hoffman et al., 2017; Clark et al., 2024).

To further examine the deglacial warming trend, we compare the warming rate per century across these three terminations using the first derivative of GMST data (**Fig. 8**). These warming rates were obtained using randomly drawn GMST values (within the 2s uncertainty for each time-bin) in a Monte-Carlo (10^5 iterations) process for each Termination. This comparison indicates that the mean rate of warming is similar for T-II and T-IV (0.03°C per century) but slightly higher for T-I (0.05°C per century). However, the distribution of observed warming rates is skewed toward higher values for T-I (99^{th} percentile ~1.1°C per century) and T-IV (99^{th} percentile ~0.5°C per century) compared to T-II (99^{th} percentile ~0.2°C per century). We suspect that differences in the resolution of GMST reconstructions contribute to these extreme warming rates observed, underscoring the importance of producing high-resolution SST syntheses to better constrain the rates of change (**Fig. 8**).

https://doi.org/10.5194/egusphere-2025-1928
Preprint. Discussion started: 8 May 2025

Deglaciations represent the most extreme natural climatic changes of the Pleistocene period (e.g. Broecker and Denton, 1990; Cheng et al., 2009; Denton et al., 2010; Cheng et al., 2016). However, present-day warming, as illustrated by the HadCRUT5 dataset (Morice et al., 2021), stands out as one of the fastest warming periods (Calvin et al., 2023). To contextualize current warming trends in the framework of past climate extremes, we calculated different warming rates from HadCRUT5 over the last 60 to 170 years (before 2023; **Fig. 8**). Notably, for T-I (Osman et al., 2021), which has the highest-resolution GMST stack, the temperature increase over the last 60 years is almost twice as high as the 99th percentile of T-I warming rates. For T-IV, the 99th percentile (~0.5°C per century) is almost three times lower than the current warming trend observed over the last 80 years. This comparison starkly highlights the exceptional nature of modern warming, which significantly outpaces the largest natural temperature changes recorded over the last 400 ka.

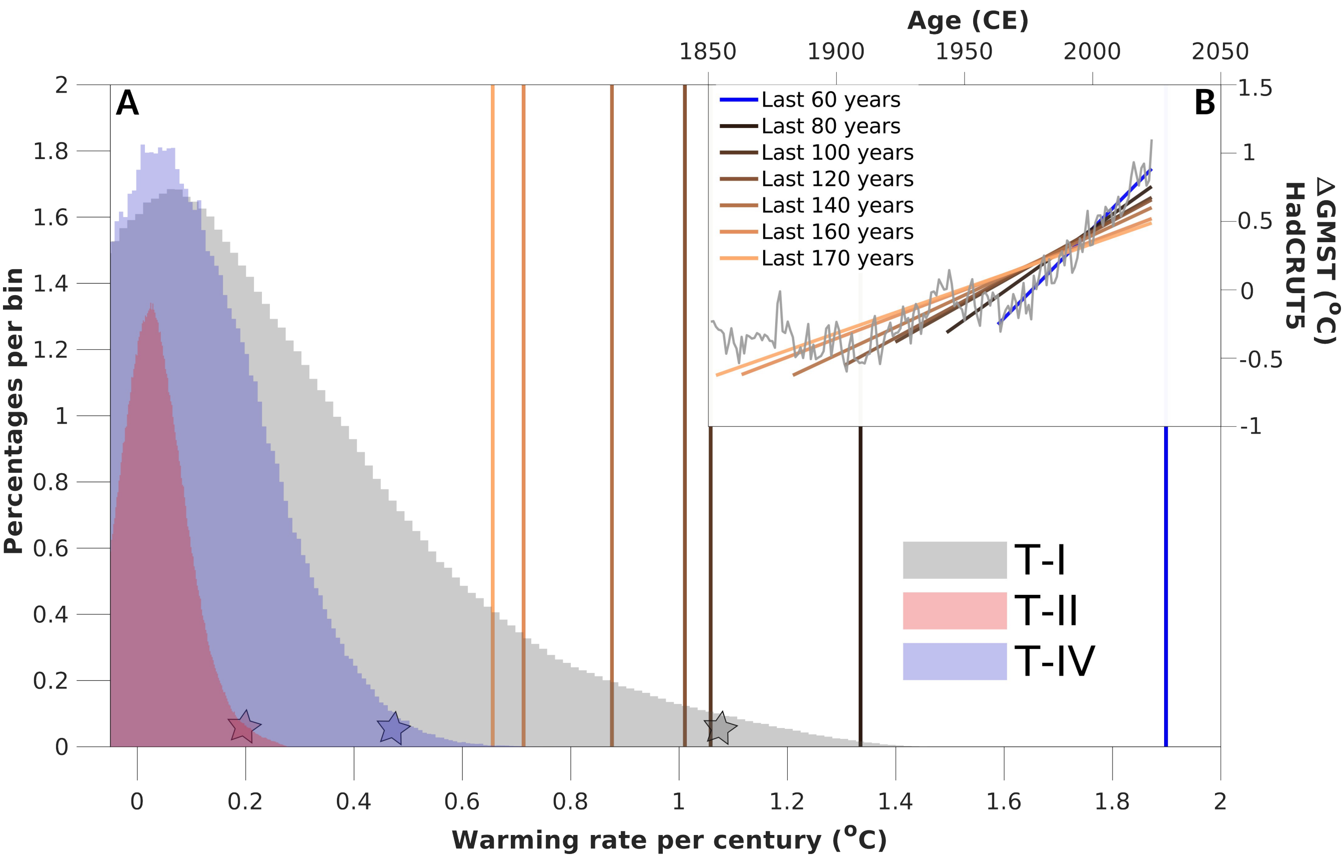

Figure 8: Percentages of rate of warming over termination I, II and IV. These rates were obtained using the first derivative with 10^5 iterations, which randomly drawn the GMST values within the 2σ uncertainty for each time-bin. Periods involved for the terminations are 20 to 10 ka (T-I, grey), 140 to 125 ka (T-II, orange) and 346 to 333.5 ka (T-IV, blue). Coloured stars represent the 99th percentile observed for each deglaciation. The insert in the right corner represents the HadCRUT5 (Morice et al., 2021) temperature curve, representative of the most recent (1850 to 2023 years CE) GMST. We calculate the warming trend, from the last 170 to the last 60 years (20 years step). Then, after a conversion in °C per century, we report these trends in the principal panel (vertical bands) for a comparison to those obtained for the three terminations.

https://doi.org/10.5194/egusphere-2025-1928
Preprint. Discussion started: 8 May 2025

5 Conclusions and perspectives

This study provides the most comprehensive SST synthesis covering MIS 9e and T-IV to date. It includes 98 marine sediment SST reconstructions and it benefits from a consistent dating between the different records as well as quantitative estimates of all source of uncertainties associated with both the chronologies and with the use of SST proxies. Hence, this compilation provides the first insights on the deglacial and interglacial surface temperature variability at both global and regional scales over this time period characterized by the highest natural CO_2 concentrations over the past 800 ka. Our results highlights the following points:

- Hemispheric temperature stacks reveal pronounced asynchrony both in the timing and magnitude of deglacial warming across regions. The extra-tropics bands are characterised by warmer optimum (~0.1 and ~0.2°C for Northern and Southern hemispheres, respectively) than intra-tropic areas (~-0.5°C), suggesting a strong polar amplification of warming. A late optimum is also observed in intra-tropic areas, more affected by external forcing than extra-tropics.
- The regional SST patterns appear to be affected by global radiative forcing at first order, but are mainly influenced by regional features as water exchanges between Atlantic and Indian ocean, meltwater discharges or changes in atmospheric and oceanic dynamics.
- We provide refined estimates of T-IV and MIS 9e ΔGMST, relying on our new synthesis that is based on a larger number of records associated with a higher temporal resolution and a more detailed chronological framework than the published compilation covering this time interval. Hence, the deglacial warming during T-IV is of ~5.6°C and reaches a maximum value of -0.4 ± 0.6°C relative to PI during the MIS 9e. Such subdued global temperature estimate results from the temporal asynchronicity of the more pronounced regional temperature changes.
- The ΔGMST reconstruction highlights that the global deglacial warming amplitude during T-IV (~5.6 °C) is comparable to the ones observed during of T-I and T-II, but MIS 9e remains cooler than the early Holocene and LIG. This muted response contrasts with the high CO_2 and CH_4 concentrations of MIS 9e peak, underscoring the need to better understand feedback mechanisms governing global and regional temperature responses.
- Despite differences in orbital configurations and GHG forcing, past interglacials exhibit recurrent patterns, such as delayed global temperature peaks relative to GHG and Antarctic temperature changes. However, while the Holocene and MIS 5e temperatures indicate a cooling after reaching the optimum, MIS 9e stands out and show a relatively stable plateau before the glacial inception.
- Comparisons of past warming rates reveal that T-IV and T-II share similar mean warming rates (~0.03°C per century), with higher extremes observed in T-I. We found that high-resolution GMST leads to a better estimation of “extreme” warming rates during deglaciations. Present-day warming rates over the last century are exceptional, far exceeding even the 99th percentile of natural variability during these three past terminations.

https://doi.org/10.5194/egusphere-2025-1928
Preprint. Discussion started: 8 May 2025

Our new results call for several future research directions to better understand mechanisms involved in past terminations and interglacials periods:

- In several instances, we found inconsistent signals from a single site with different SST estimates derived from different proxies. Despite the recent improvements in SST calibrations, the lack of prior parameters (e.g. seawater properties) needed for calibrations leads to these inconsistent temporal variabilities or absolute SST values. Efforts should be made to produce more estimations of past seawater properties data to better constrain the SST calibrations.
- High-resolution SST records from polar and subpolar regions are essential to resolve the spatial variability and constrain the role of high-latitude processes in interglacial climates. Additionally, integrating paleo-proxies for AMOC dynamics would address key uncertainties about its role in modulating heat transport and carbon cycles.
- Comparing the MIS 9e ΔGMST to existing MIS 5e and Holocene GMST provides insights on our understanding of past climate response during warm intervals associated with slightly different forcing. Additional syntheses should cover more interglacials and Terminations to progress on our understanding of the dynamics and the diversity of the Quaternary interglacials.
- This new compilation is a useful benchmark to evaluate ESM simulations that have been performed over this time interval. Such data-model comparisons would enable to disentangle the interplay between orbital forcing, GHG variations or ocean dynamics over this period.
- Data assimilation offers a transformational approach to paleoclimate studies by integrating disparate proxy datasets with climate model outputs, enabling temporally and spatially complete reconstructions. Its application with our new MIS 9 synthesis could reduce biases arising from uneven proxy coverage and improve the determination of the global and regional climate patterns.

Finally, T-IV and MIS 9e illustrate the complexity of natural climate transitions, driven by a combination of orbital dynamics, greenhouse gas forcing, and ocean-atmosphere feedbacks. While these processes produced significant climatic shifts over millennia, their magnitude and pace are minimal compared to the current anthropogenic warming. By contextualizing modern warming within the late Quaternary framework of Earth's climatic history, this study reaffirms the extraordinary nature of the current anthropogenic warming and the urgent need for decisive action to mitigate its impacts.

Acknowledgements

This study is an outcome of the Make Our Planet Great Again HOTCLIM project; it received the financial support from the French National Research Agency under the ‘Programme d’Investissements d’Avenir’ (ANR-19-MPGA-0001). We thank all authors who kindly shared their SST datasets with us, *via* personal communication or by the way of international FAIR database. We also thank Frédérique Parrenin for fruitful discussions about the chronological aspect of this study.

Data availability

All references of data used in this synthesis are listed in **Table S2**. The revised age models, SST and tie-points will be published in the PANGAEA database.

Authors contributions

NS and EC designed the research. NS collected the datasets building on a preliminary effort undertaken by CC. NS computed age models, SST calibrations and developed the method to infer the global and regional temperature stacks. NS lead the writing of the manuscript with subsequent inputs from EC and EL.

References

Anand, P., Elderfield, H., and Conte, M. H.: Calibration of Mg/Ca thermometry in planktonic foraminifera from a sediment trap time series, Paleoceanography, 18, 2002PA000846, https://doi.org/10.1029/2002PA000846, 2003.

Bard, E. and Rickaby, R. E. M.: Migration of the subtropical front as a modulator of glacial climate, Nature, 460, 380–383, https://doi.org/10.1038/nature08189, 2009.

Barker, S., Knorr, G., Edwards, R. L., Parrenin, F., Putnam, A. E., Skinner, L. C., Wolff, E., and Ziegler, M.: 800,000 Years of Abrupt Climate Variability, Science, 334, 347–351, https://doi.org/10.1126/science.1203580, 2011.

Barker, S., Chen, J., Gong, X., Jonkers, L., Knorr, G., and Thornalley, D.: Icebergs not the trigger for North Atlantic cold events, Nature, 520, 333–336, https://doi.org/10.1038/nature14330, 2015.

Beal, L. M., De Ruijter, W. P. M., Biastoch, A., Zahn, R., SCOR/WCRP/IAPSO Working Group 136, Cronin, M., Hermes, J., Lutjeharms, J., Quartly, G., Tozuka, T., Baker-Yeboah, S., Bornman, T., Cipollini, P., Dijkstra, H., Hall, I., Park, W., Peeters, F., Penven, P., Ridderinkhof, H., and Zinke, J.: On the role of the Agulhas system in ocean circulation and climate, Nature, 472, 429–436, https://doi.org/10.1038/nature09983, 2011.

Bereiter, B., Eggleston, S., Schmitt, J., Nehrbass-Ahles, C., Stocker, T. F., Fischer, H., Kipfstuhl, S., and Chappellaz, J.: Revision of the EPICA Dome C CO 2 record from 800 to 600 kyr before present, Geophysical Research Letters, 42, 542–549, https://doi.org/10.1002/2014GL061957, 2015.

Berger, A. and Loutre, M. F.: Insolation values for the climate of the last 10 million years, Quaternary Science Reviews, 10, 297–317, https://doi.org/10.1016/0277-3791(91)90033-Q, 1991.

Biastoch, A., Böning, C. W., Schwarzkopf, F. U., and Lutjeharms, J. R. E.: Increase in Agulhas leakage due to poleward shift of Southern Hemisphere westerlies, Nature, 462, 495–498, https://doi.org/10.1038/nature08519, 2009.

Bouchet, M., Landais, A., Grisart, A., Parrenin, F., Prié, F., Jacob, R., Fourré, E., Capron, E., Raynaud, D., Lipenkov, V. Y., Loutre, M.-F., Extier, T., Svensson, A., Legrain, E., Martinerie, P., Leuenberger, M., Jiang, W., Ritterbusch, F., Lu, Z.-T., and Yang, G.-M.: The Antarctic Ice Core Chronology 2023 (AICC2023) chronological framework and

https://doi.org/10.5194/egusphere-2025-1928
Preprint. Discussion started: 8 May 2025

associated timescale for the European Project for Ice Coring in Antarctica (EPICA) Dome C ice core, Clim. Past, 19, 2257–2286, https://doi.org/10.5194/cp-19-2257-2023, 2023.

Bouttes, N., Vazquez Riveiros, N., Govin, A., Swingedouw, D., Sanchez-Goni, M. F., Crosta, X., and Roche, D. M.: Carbon 13 Isotopes Reveal Limited Ocean Circulation Changes Between Interglacials of the Last 800 ka, Paleoceanog and Paleoclimatol, 35, e2019PA003776, https://doi.org/10.1029/2019PA003776, 2020.

Broecker, W. S. and Denton, G. H.: The role of ocean-atmosphere reorganizations in glacial cycles, Quaternary Science Reviews, 9, 305–341, https://doi.org/10.1016/0277-3791(90)90026-7, 1990.

Caley, T., Kim, J.-H., Malaizé, B., Giraudeau, J., Laepple, T., Caillon, N., Charlier, K., Rebaubier, H., Rossignol, L., Castañeda, I. S., Schouten, S., and Sinninghe Damsté, J. S.: High-latitude obliquity as a dominant forcing in the Agulhas current system, Clim. Past, 7, 1285–1296, https://doi.org/10.5194/cp-7-1285-2011, 2011.

Caley, T., Giraudeau, J., Malaizé, B., Rossignol, L., and Pierre, C.: Agulhas leakage as a key process in the modes of Quaternary climate changes, Proc. Natl. Acad. Sci. U.S.A., 109, 6835–6839, https://doi.org/10.1073/pnas.1115545109, 2012.

Capron, E., Govin, A., Stone, E. J., Masson-Delmotte, V., Mulitza, S., Otto-Bliesner, B., Rasmussen, T. L., Sime, L. C., Waelbroeck, C., and Wolff, E. W.: Temporal and spatial structure of multi-millennial temperature changes at high latitudes during the Last Interglacial, Quaternary Science Reviews, 103, 116–133, https://doi.org/10.1016/j.quascirev.2014.08.018, 2014.

Capron, E., Govin, A., Feng, R., Otto-Bliesner, B. L., and Wolff, E. W.: Critical evaluation of climate syntheses to benchmark CMIP6/PMIP4 127 ka Last Interglacial simulations in the high-latitude regions, Quaternary Science Reviews, 168, 137–150, https://doi.org/10.1016/j.quascirev.2017.04.019, 2017.

Capron, E., Rovere, A., Austermann, J., Axford, Y., Barlow, N. L. M., Carlson, A. E., De Vernal, A., Dutton, A., Kopp, R. E., McManus, J. F., Menviel, L., Otto-Bliesner, B. L., Robinson, A., Shakun, J. D., Tzedakis, P. C., and Wolff, E. W.: Challenges and research priorities to understand interactions between climate, ice sheets and global mean sea level during past interglacials, Quaternary Science Reviews, 219, 308–311, https://doi.org/10.1016/j.quascirev.2019.06.030, 2019.

Cheng, H., Edwards, R. L., Broecker, W. S., Denton, G. H., Kong, X., Wang, Y., Zhang, R., and Wang, X.: Ice Age Terminations, Science, 326, 248–252, https://doi.org/10.1126/science.1177840, 2009.

Cheng, H., Edwards, R. L., Sinha, A., Spötl, C., Yi, L., Chen, S., Kelly, M., Kathayat, G., Wang, X., Li, X., Kong, X., Wang, Y., Ning, Y., and Zhang, H.: The Asian monsoon over the past 640,000 years and ice age terminations, Nature, 534, 640–646, https://doi.org/10.1038/nature18591, 2016.

Clark, P. U., Shakun, J. D., Rosenthal, Y., Köhler, P., and Bartlein, P. J.: Global and regional temperature change over the past 4.5 million years, Science, 383, 884–890, https://doi.org/10.1126/science.adi1908, 2024.

Clemens, S. C., Holbourn, A., Kubota, Y., Lee, K. E., Liu, Z., Chen, G., Nelson, A., and Fox-Kemper, B.: Precession-band variance missing from East Asian monsoon runoff, Nat Commun, 9, 3364, https://doi.org/10.1038/s41467-018-05814-0, 2018.

Davtian, N. and Bard, E.: A new view on abrupt climate changes and the bipolar seesaw based on paleotemperatures from Iberian Margin sediments, Proc. Natl. Acad. Sci. U.S.A., 120, e2209558120, https://doi.org/10.1073/pnas.2209558120, 2023.

Denton, G. H., Anderson, R. F., Toggweiler, J. R., Edwards, R. L., Schaefer, J. M., and Putnam, A. E.: The Last Glacial Termination, Science, 328, 1652–1656, https://doi.org/10.1126/science.1184119, 2010.

Denton, G. H., Putnam, A. E., Russell, J. L., Barrell, D. J. A., Schaefer, J. M., Kaplan, M. R., and Strand, P. D.: The Zealandia Switch: Ice age climate shifts viewed from Southern Hemisphere moraines, Quaternary Science Reviews, 257, 106771, https://doi.org/10.1016/j.quascirev.2020.106771, 2021.

Friedrich, T., Timmermann, A., Tigchelaar, M., Elison Timm, O., and Ganopolski, A.: Nonlinear climate sensitivity and its implications for future greenhouse warming, Sci. Adv., 2, e1501923, https://doi.org/10.1126/sciadv.1501923, 2016.

Gao, Q., Capron, E., Sime, L. C., Rhodes, R. H., Sivankutty, R., Zhang, X., Otto-Bliesner, B. L., and Werner, M.: Assessment of the southern polar and subpolar warming in the PMIP4 Last Interglacial simulations using paleoclimate data syntheses, https://doi.org/10.5194/egusphere-2024-1261, 7 May 2024.

Govin, A., Braconnot, P., Capron, E., Cortijo, E., Duplessy, J.-C., Jansen, E., Labeyrie, L., Landais, A., Marti, O., Michel, E., Mosquet, E., Risebrobakken, B., Swingedouw, D., and Waelbroeck, C.: Persistent influence of ice sheet melting on high northern latitude climate during the early Last Interglacial, Clim. Past, 8, 483–507, https://doi.org/10.5194/cp-8-483-2012, 2012.

Govin, A., Capron, E., Tzedakis, P. C., Verheyden, S., Ghaleb, B., Hillaire-Marcel, C., St-Onge, G., Stoner, J. S., Bassinot, F., Bazin, L., Blunier, T., Combourieu-Nebout, N., El Ouahabi, A., Genty, D., Gersonde, R., Jimenez-Amat, P., Landais, A., Martrat, B., Masson-Delmotte, V., Parrenin, F., Seidenkrantz, M.-S., Veres, D., Waelbroeck, C., and Zahn, R.: Sequence of events from the onset to the demise of the Last Interglacial: Evaluating strengths and limitations of chronologies used in climatic archives, Quaternary Science Reviews, 129, 1–36, https://doi.org/10.1016/j.quascirev.2015.09.018, 2015.

Grant, K. M., Rohling, E. J., Ramsey, C. B., Cheng, H., Edwards, R. L., Florindo, F., Heslop, D., Marra, F., Roberts, A. P., Tamisiea, M. E., and Williams, F.: Sea-level variability over five glacial cycles, Nat Commun, 5, 5076, https://doi.org/10.1038/ncomms6076, 2014.

Gray, W. R. and Evans, D.: Nonthermal Influences on Mg/Ca in Planktonic Foraminifera: A Review of Culture Studies and Application to the Last Glacial Maximum, Paleoceanog and Paleoclimatol, 34, 306–315, https://doi.org/10.1029/2018PA003517, 2019.

https://doi.org/10.5194/egusphere-2025-1928
Preprint. Discussion started: 8 May 2025

Gray, W. R., Weldeab, S., Lea, D. W., Rosenthal, Y., Gruber, N., Donner, B., and Fischer, G.: The effects of temperature, salinity, and the carbonate system on Mg/Ca in Globigerinoides ruber (white): A global sediment trap calibration, Earth and Planetary Science Letters, 482, 607–620, https://doi.org/10.1016/j.epsl.2017.11.026, 2018.

Gray, W. R., De Lavergne, C., Jnglin Wills, R. C., Menviel, L., Spence, P., Holzer, M., Kageyama, M., and Michel, E.: Poleward Shift in the Southern Hemisphere Westerly Winds Synchronous With the Deglacial Rise in CO 2, Paleoceanog and Paleoclimatol, 38, e2023PA004666, https://doi.org/10.1029/2023PA004666, 2023.

Haeberli, M., Baggenstos, D., Schmitt, J., Grimmer, M., Michel, A., Kellerhals, T., and Fischer, H.: Snapshots of mean ocean temperature over the last 700 000 years using noble gases in the EPICA Dome C ice core, Clim. Past, 17, 843–867, https://doi.org/10.5194/cp-17-843-2021, 2021.

Henry, L. G., McManus, J. F., Curry, W. B., Roberts, N. L., Piotrowski, A. M., and Keigwin, L. D.: North Atlantic ocean circulation and abrupt climate change during the last glaciation, Science, 353, 470–474, https://doi.org/10.1126/science.aaf5529, 2016.

Hodell, D. A., Crowhurst, S. J., Lourens, L., Margari, V., Nicolson, J., Rolfe, J. E., Skinner, L. C., Thomas, N. C., Tzedakis, P. C., Mleneck-Vautravers, M. J., and Wolff, E. W.: A 1.5-million-year record of orbital and millennial climate variability in the North Atlantic, Clim. Past, 19, 607–636, https://doi.org/10.5194/cp-19-607-2023, 2023.

Hodell, D., Lourens, L., Crowhurst, S., Konijnendijk, T., Tjallingii, R., Jiménez-Espejo, F., Skinner, L., Tzedakis, P. C., Abrantes, F., Acton, G. D., Alvarez Zarikian, C. A., Bahr, A., Balestra, B., Barranco, E. L., Carrara, G., Ducassou, E., Flood, R. D., Flores, J.-A., Furota, S., Grimalt, J., Grunert, P., Hernández-Molina, J., Kim, J. K., Krissek, L. A., Kuroda, J., Li, B., Lofi, J., Margari, V., Martrat, B., Miller, M. D., Nanayama, F., Nishida, N., Richter, C., Rodrigues, T., Rodríguez-Tovar, F. J., Roque, A. C. F., Sanchez Goñi, M. F., Sierro Sánchez, F. J., Singh, A. D., Sloss, C. R., Stow, D. A. V., Takashimizu, Y., Tzanova, A., Voelker, A., Xuan, C., and Williams, T.: A reference time scale for Site U1385 (Shackleton Site) on the SW Iberian Margin, Global and Planetary Change, 133, 49–64, https://doi.org/10.1016/j.gloplacha.2015.07.002, 2015.

Hoffman, J. S., Clark, P. U., Parnell, A. C., and He, F.: Regional and global sea-surface temperatures during the last interglaciation, Science, 355, 276–279, https://doi.org/10.1126/science.aai8464, 2017.

Holland, M. M. and Bitz, C. M.: Polar amplification of climate change in coupled models, Climate Dynamics, 21, 221–232, https://doi.org/10.1007/s00382-003-0332-6, 2003.

Jouzel, J., Masson-Delmotte, V., Cattani, O., Dreyfus, G., Falourd, S., Hoffmann, G., Minster, B., Nouet, J., Barnola, J. M., Chappellaz, J., Fischer, H., Gallet, J. C., Johnsen, S., Leuenberger, M., Loulergue, L., Luethi, D., Oerter, H., Parrenin, F., Raisbeck, G., Raynaud, D., Schilt, A., Schwander, J., Selmo, E., Souchez, R., Spahni, R., Stauffer, B., Steffensen, J. P., Stenni, B., Stocker, T. F., Tison, J. L., Werner, M., and Wolff, E. W.: Orbital and Millennial Antarctic Climate Variability over the Past 800,000 Years, Science, 317, 793–796, https://doi.org/10.1126/science.1141038, 2007.

Lamy, F., Winckler, G., Arz, H. W., Farmer, J. R., Gottschalk, J., Lembke-Jene, L., Middleton, J. L., Van Der Does, M., Tiedemann, R., Alvarez Zarikian, C., Basak, C., Brombacher, A., Dumm, L., Esper, O. M., Herbert, L. C., Iwasaki, S., Kreps, G., Lawson, V. J., Lo, L., Malinverno, E., Martinez-Garcia, A., Michel, E., Moretti, S., Moy, C. M., Ravelo, A. C., Riesselman, C. R., Saavedra-Pellitero, M., Sadatzki, H., Seo, I., Singh, R. K., Smith, R. A., Souza, A. L., Stoner, J. S., Toyos, M., De Oliveira, I. M. V. P., Wan, S., Wu, S., and Zhao, X.: Five million years of Antarctic Circumpolar Current strength variability, Nature, 627, 789–796, https://doi.org/10.1038/s41586-024-07143-3, 2024.

Landais, A., Stenni, B., Masson-Delmotte, V., Jouzel, J., Cauquoin, A., Fourré, E., Minster, B., Selmo, E., Extier, T., Werner, M., Vimeux, F., Uemura, R., Crotti, I., and Grisart, A.: Interglacial Antarctic–Southern Ocean climate decoupling due to moisture source area shifts, Nat. Geosci., 14, 918–923, https://doi.org/10.1038/s41561-021-00856-4, 2021.

Laskar, J., Robutel, P., Joutel, F., Gastineau, M., Correia, A. C. M., and Levrard, B.: A long-term numerical solution for the insolation quantities of the Earth, A&A, 428, 261–285, https://doi.org/10.1051/0004-6361:20041335, 2004.

Legrain, E., Capron, E., Menviel, L., Wohleber, A., Parrenin, F., Teste, G., Landais, A., Bouchet, M., Grilli, R., Nehrbass-Ahles, C., Silva, L., Fischer, H., and Stocker, T. F.: Centennial-scale variations in the carbon cycle enhanced by high obliquity, Nat. Geosci., 17, 1154–1161, https://doi.org/10.1038/s41561-024-01556-5, 2024.

LeGrande, A. N. and Schmidt, G. A.: Global gridded data set of the oxygen isotopic composition in seawater, Geophysical Research Letters, 33, 2006GL026011, https://doi.org/10.1029/2006GL026011, 2006.

Lisiecki, L. E. and Raymo, M. E.: A Pliocene-Pleistocene stack of 57 globally distributed benthic δ 18 O records, Paleoceanography, 20, 2004PA001071, https://doi.org/10.1029/2004PA001071, 2005.

Lougheed, B. C. and Obrochta, S. P.: A Rapid, Deterministic Age-Depth Modeling Routine for Geological Sequences With Inherent Depth Uncertainty, Paleoceanog and Paleoclimatol, 34, 122–133, https://doi.org/10.1029/2018PA003457, 2019.

Loulergue, L., Schilt, A., Spahni, R., Masson-Delmotte, V., Blunier, T., Lemieux, B., Barnola, J.-M., Raynaud, D., Stocker, T. F., and Chappellaz, J.: Orbital and millennial-scale features of atmospheric CH4 over the past 800,000 years, Nature, 453, 383–386, https://doi.org/10.1038/nature06950, 2008.

Lynch-Stieglitz, J.: The Atlantic Meridional Overturning Circulation and Abrupt Climate Change, Annu. Rev. Mar. Sci., 9, 83–104, https://doi.org/10.1146/annurev-marine-010816-060415, 2017.

Malevich, S. B., Vetter, L., and Tierney, J. E.: Global Core Top Calibration of δ 18 O in Planktic Foraminifera to Sea Surface Temperature, Paleoceanog and Paleoclimatol, 34, 1292–1315, https://doi.org/10.1029/2019PA003576, 2019.

Martrat, B., Grimalt, J. O., Shackleton, N. J., De Abreu, L., Hutterli, M. A., and Stocker, T. F.: Four Climate Cycles of Recurring Deep and Surface Water Destabilizations on the Iberian Margin, Science, 317, 502–507, https://doi.org/10.1126/science.1139994, 2007.

Masson-Delmotte, V., Stenni, B., Blunier, T., Cattani, O., Chappellaz, J., Cheng, H., Dreyfus, G., Edwards, R. L., Falourd, S., Govin, A., Kawamura, K., Johnsen, S. J., Jouzel, J., Landais, A., Lemieux-Dudon, B., Lourantou, A., Marshall, G., Minster, B., Mudelsee, M., Pol, K., Röthlisberger, R., Selmo, E., and Waelbroeck, C.: Abrupt change of Antarctic

https://doi.org/10.5194/egusphere-2025-1928
Preprint. Discussion started: 8 May 2025

moisture origin at the end of Termination II, Proc. Natl. Acad. Sci. U.S.A., 107, 12091–12094, https://doi.org/10.1073/pnas.0914536107, 2010.

McManus, J. F., Oppo, D. W., and Cullen, J. L.: A 0.5-Million-Year Record of Millennial-Scale Climate Variability in the North Atlantic, Science, 283, 971–975, https://doi.org/10.1126/science.283.5404.971, 1999.

McManus, J. F., Francois, R., Gherardi, J.-M., Keigwin, L. D., and Brown-Leger, S.: Collapse and rapid resumption of Atlantic meridional circulation linked to deglacial climate changes, Nature, 428, 834–837, https://doi.org/10.1038/nature02494, 2004.

Medina-Elizalde, M.: A global compilation of coral sea-level benchmarks: Implications and new challenges, Earth and Planetary Science Letters, 362, 310–318, https://doi.org/10.1016/j.epsl.2012.12.001, 2013.

Morice, C. P., Kennedy, J. J., Rayner, N. A., Winn, J. P., Hogan, E., Killick, R. E., Dunn, R. J. H., Osborn, T. J., Jones, P. D., and Simpson, I. R.: An Updated Assessment of Near-Surface Temperature Change From 1850: The HadCRUT5 Data Set, JGR Atmospheres, 126, e2019JD032361, https://doi.org/10.1029/2019JD032361, 2021.

Nehrbass-Ahles, C., Shin, J., Schmitt, J., Bereiter, B., Joos, F., Schilt, A., Schmidely, L., Silva, L., Teste, G., Grilli, R., Chappellaz, J., Hodell, D., Fischer, H., and Stocker, T. F.: Abrupt CO 2 release to the atmosphere under glacial and early interglacial climate conditions, Science, 369, 1000–1005, https://doi.org/10.1126/science.aay8178, 2020.

Nuber, S., Rae, J. W. B., Zhang, X., Andersen, M. B., Dumont, M. D., Mithan, H. T., Sun, Y., De Boer, B., Hall, I. R., and Barker, S.: Indian Ocean salinity build-up primes deglacial ocean circulation recovery, Nature, 617, 306–311, https://doi.org/10.1038/s41586-023-05866-3, 2023.

Osman, M. B., Tierney, J. E., Zhu, J., Tardif, R., Hakim, G. J., King, J., and Poulsen, C. J.: Globally resolved surface temperatures since the Last Glacial Maximum, Nature, 599, 239–244, https://doi.org/10.1038/s41586-021-03984-4, 2021.

Paillard, D., Labeyrie, L., and Yiou, P.: Macintosh Program performs time-series analysis, EoS Transactions, 77, 379–379, https://doi.org/10.1029/96EO00259, 1996.

Past Interglacials Working Group of PAGES: Interglacials of the last 800,000 years, Reviews of Geophysics, 54, 162–219, https://doi.org/10.1002/2015RG000482, 2016.

Pedro, J. B., Jochum, M., Buizert, C., He, F., Barker, S., and Rasmussen, S. O.: Beyond the bipolar seesaw: Toward a process understanding of interhemispheric coupling, Quaternary Science Reviews, 192, 27–46, https://doi.org/10.1016/j.quascirev.2018.05.005, 2018.

Peeters, F. J. C., Acheson, R., Brummer, G.-J. A., De Ruijter, W. P. M., Schneider, R. R., Ganssen, G. M., Ufkes, E., and Kroon, D.: Vigorous exchange between the Indian and Atlantic oceans at the end of the past five glacial periods, Nature, 430, 661–665, https://doi.org/10.1038/nature02785, 2004.

Prahl, F. G., Muehlhausen, L. A., and Zahnle, D. L.: Further evaluation of long-chain alkenones as indicators of paleoceanographic conditions, Geochimica et Cosmochimica Acta, 52, 2303–2310, https://doi.org/10.1016/0016-7037(88)90132-9, 1988.

https://doi.org/10.5194/egusphere-2025-1928
Preprint. Discussion started: 8 May 2025

Rayner, N. A., Parker, D. E., Horton, E. B., Folland, C. K., Alexander, L. V., Rowell, D. P., Kent, E. C., and Kaplan, A.: Global analyses of sea surface temperature, sea ice, and night marine air temperature since the late nineteenth century, J. Geophys. Res., 108, 2002JD002670, https://doi.org/10.1029/2002JD002670, 2003.

Rouyer-Denimal, L., Govin, A., Bouloubassi, I., Nguyen Tu, T. T., Albuquerque, A. L. S., Anquetil, C., and Huguet, A.: Subsurface warming in the tropical Atlantic for the last 3 deglaciations: Insights from organic molecular proxies, Quaternary Science Reviews, 321, 108370, https://doi.org/10.1016/j.quascirev.2023.108370, 2023.

Shackleton, S., Baggenstos, D., Menking, J. A., Dyonisius, M. N., Bereiter, B., Bauska, T. K., Rhodes, R. H., Brook, E. J., Petrenko, V. V., McConnell, J. R., Kellerhals, T., Häberli, M., Schmitt, J., Fischer, H., and Severinghaus, J. P.: Global ocean heat content in the Last Interglacial, Nat. Geosci., 13, 77–81, https://doi.org/10.1038/s41561-019-0498-0, 2020.

Shakun, J. D., Clark, P. U., He, F., Marcott, S. A., Mix, A. C., Liu, Z., Otto-Bliesner, B., Schmittner, A., and Bard, E.: Global warming preceded by increasing carbon dioxide concentrations during the last deglaciation, Nature, 484, 49–54, https://doi.org/10.1038/nature10915, 2012.

Shakun, J. D., Lea, D. W., Lisiecki, L. E., and Raymo, M. E.: An 800-kyr record of global surface ocean δ 18 O and implications for ice volume-temperature coupling, Earth and Planetary Science Letters, 426, 58–68, https://doi.org/10.1016/j.epsl.2015.05.042, 2015.

Sigman, D. M., Hain, M. P., and Haug, G. H.: The polar ocean and glacial cycles in atmospheric CO2 concentration, Nature, 466, 47–55, https://doi.org/10.1038/nature09149, 2010.

Snyder, C. W.: Evolution of global temperature over the past two million years, Nature, 538, 226–228, https://doi.org/10.1038/nature19798, 2016.

Spratt, R. M. and Lisiecki, L. E.: A Late Pleistocene sea level stack, Clim. Past, 12, 1079–1092, https://doi.org/10.5194/cp-12-1079-2016, 2016.

Stevenard, N., Kissel, C., Govin, A., and Wandres, C.: Deep north atlantic circulation strength: Glacial-interglacial variability over the last 400,000 years, Quaternary Science Reviews, 345, 109011, https://doi.org/10.1016/j.quascirev.2024.109011, 2024.

Stocker, T. F. and Johnsen, S. J.: A minimum thermodynamic model for the bipolar seesaw, Paleoceanography, 18, 2003PA000920, https://doi.org/10.1029/2003PA000920, 2003.

Stommel, H.: Thermohaline Convection with Two Stable Regimes of Flow, Tellus, 13, 224–230, https://doi.org/10.1111/j.2153-3490.1961.tb00079.x, 1961.

Stone, E. J., Capron, E., Lunt, D. J., Payne, A. J., Singarayer, J. S., Valdes, P. J., and Wolff, E. W.: Impact of meltwater on high-latitude early Last Interglacial climate, Clim. Past, 12, 1919–1932, https://doi.org/10.5194/cp-12-1919-2016, 2016.

Tierney, J. E. and Tingley, M. P.: BAYSPLINE: A New Calibration for the Alkenone Paleothermometer, Paleoceanog and Paleoclimatol, 33, 281–301, https://doi.org/10.1002/2017PA003201, 2018.

Tierney, J. E., Malevich, S. B., Gray, W., Vetter, L., and Thirumalai, K.: Bayesian Calibration of the Mg/Ca Paleothermometer in Planktic Foraminifera, Paleoceanog and Paleoclimatol, 34, 2005–2030, https://doi.org/10.1029/2019PA003744, 2019.

Tierney, J. E., Zhu, J., King, J., Malevich, S. B., Hakim, G. J., and Poulsen, C. J.: Glacial cooling and climate sensitivity revisited, Nature, 584, 569–573, https://doi.org/10.1038/s41586-020-2617-x, 2020.

Turney, C. S. M. and Jones, R. T.: Does the Agulhas Current amplify global temperatures during super-interglacials?, J Quaternary Science, 25, 839–843, https://doi.org/10.1002/jqs.1423, 2010.

Tzedakis, P. C., Wolff, E. W., Skinner, L. C., Brovkin, V., Hodell, D. A., McManus, J. F., and Raynaud, D.: Can we predict the duration of an interglacial?, Clim. Past, 8, 1473–1485, https://doi.org/10.5194/cp-8-1473-2012, 2012.

Wassenburg, J. A., Vonhof, H. B., Cheng, H., Martínez-García, A., Ebner, P.-R., Li, X., Zhang, H., Sha, L., Tian, Y., Edwards, R. L., Fiebig, J., and Haug, G. H.: Penultimate deglaciation Asian monsoon response to North Atlantic circulation collapse, Nat. Geosci., https://doi.org/10.1038/s41561-021-00851-9, 2021.

Yin, Q. Z., Wu, Z. P., Berger, A., Goosse, H., and Hodell, D.: Insolation triggered abrupt weakening of Atlantic circulation at the end of interglacials, Science, 373, 1035–1040, https://doi.org/10.1126/science.abg1737, 2021.

Zhang, X., Knorr, G., Lohmann, G., and Barker, S.: Abrupt North Atlantic circulation changes in response to gradual CO2 forcing in a glacial climate state, Nature Geosci, 10, 518–523, https://doi.org/10.1038/ngeo2974, 2017.